X-BASE: the first terrestrial carbon and water flux products from an extended data-driven scaling framework, FLUXCOM-X

Jacob A Nelson[1,*], Sophia Walther[1,*], Fabian Gans[1], Basil Kraft[1], Ulrich Weber[1], Kimberly Novick[2], Nina Buchmann[3], Mirco Migliavacca[4], Georg Wohlfahrt[5], Ladislav Šigut[6], Andreas Ibrom[7], Dario Papale[8,9], Mathias Göckede[1], Gregory Duveiller[1], Alexander Knohl[10,11], Lukas Hörtnagl[3], Russell L. Scott[12], Weijie Zhang[1], Zayd Mahmoud Hamdi[1], Markus Reichstein[1,13], Sergio Aranda-Barranco[14,15], Jonas Ardö[16], Maarten Op de Beeck[17,18], Dave Billesbach[19], David Bowling[20], Rosvel Bracho[21], Christian Brümmer[22], Gustau Camps-Valls[23], Shiping Chen[24], Jamie Rose Cleverly[25], Ankur Desai[26], Gang Dong[27], Tarek S. El-Madany[1], Eugenie Susanne Euskirchen[28], Iris Feigenwinter[3], Marta Galvagno[29], Giacomo Al. Gerosa[30], Bert Gielen[31], Ignacio Goded[4], Sarah Goslee[32], Christopher Michael Gough[33], Bernard Heinesch[34], Kazuhito Ichii[35], Marcin Antoni Jackowicz-Korczynski[36,37], Anne Klosterhalfen[38], Sara Knox[39,40], Hideki Kobayashi[41], Kukka-Maaria Kohonen[3], Mika Korkiakoski[42], Ivan Mammarella[43], Mana Gharun[44], Riccardo Marzuoli[30], Roser Matamala[45,46,47], Stefan Metzger[48,49], Leonardo Montagnani[50], Giacomo Nicolini[9,58], Thomas O'Halloran[51,52], Jean-Marc Ourcival[53], Matthias Peichl[54], Elise Pendall[55], Borja Ruiz Reverter[56], Marilyn Roland[57], Simone Sabbatini[9,58], Torsten Sachs[59], Marius Schmidt[60], Christopher R Schwalm[61], Ankit Shekhar[3], Richard Silberstein[62], Maria Lucia Silveira[63], Donatella Spano[64,9], Torbern Tagesson[16,65], Gianluca Tramontana[66], Carlo Trotta[9], Fabio Turco[3], Timo Vesala[67,68], Caroline Vincke[69], Domenico Vitale[70], Enrique R. Vivoni[71,72], Yi Wang[3], William Woodgate[73,74], Enrico A. Yepez[75], Junhui Zhang[76,77], Donatella Zona[78], and Martin Jung[1]

[*]These authors contributed equally to this work.
[1]Max-Planck-Institute for Biogeochemistry, Germany
[2]O'Neill School of Public and Environmental Affairs, Indiana University - Bloomington (USA)
[3]Department of Environmental Systems Science, ETH Zurich, 8092 Zurich, Switzerland
[4]European Commission, Joint Research Centre, Ispra (Varese), Italy
[5]Universität Innsbruck, Institut für Ökologie, Sternwartestr. 15, 6020 Innsbruck, AUSTRIA
[6]Global Change Research Institute CAS, Bělidla 986/4a, CZ-60300 Brno, Czech Republic
[7]Department of Environment and Resource Engineering, Technical University of Denmark (DTU), Bygningstorvet 115, 2800 Kgs. Lyngby, Denmark
[8]Research Institute on Terrestrial Ecosystems (IRET), National Research Council (CNR), 00010 Montelibretti (Roma), Italy
[9]CMCC Foundation - Euro-Mediterranean Center on Climate Change, Italy
[10]University of Goettingen, Bioclimatology, Faculty of Forest Sciences, 37077 Göttingen, Germany.
[11]University of Goettingen, Centre of Biodiversity and Sustainable Land Use (CBL), 37077 Göttingen, Germany
[12]Southwest Watershed Research Center, USDA-ARS, Tucson, AZ
[13]German Centre for Integrative Biodiversity Research (iDiv) Halle–Jena–Leipzig, Leipzig, Germany
[14]Department of Ecology, University of Granada, Granada, Spain
[15]Andalusian Institute for Earth System Research (CEAMA-IISTA), University of Granada, Granada, Spain
[16]Department of Physical Geography and Ecosystem Science, Lund University, Sölvegatan 12 223 62 Lund, Sweden
[17]Research Group Plants and Ecosystems, Department of Biology, University of Antwerp
[18]ICOS / Ecosystem Thematic Centre
[19]University of Nebraska-Lincoln, School of Natural Resources (Retired)

[20]School of Biological Sciences, University of Utah

[21]School of Forest, Fisheries, and Geomatics Sciences University of Florida, Gainesville, FL,32611, USA

[22]Thünen Institute of Climate-Smart Agriculture, Braunschweig, Germany

[23]Image Processing Laboratory (IPL), Universitat de València, Spain

[24]State Key Laboratory of Vegetation and Environmental Change, Institute of Botany, Chinese Academy of Sciences, Beijing 100093, P. R. China

[25]College of Science and Engineering, James Cook University, Cairns, Queensland, Australia

[26]Dept of Atmospheric and Oceanic Sciences, University of Wisconsin-Madison, Madison, WI 53706 USA

[27]Shanxi University, China

[28]University of Alaska Fairbanks, Institute of Arctic Biology, Fairbanks, AK 99775, USA

[29]Environmental Protection Agency of Aosta Valley, Climate Change Unit, (ARPA Valle d'Aosta), Italy

[30]Dept. of Mathematics and Physics, Catholic University of the Sacred Heart, Brescia (Italy)

[31]Plants and Ecosystems (PLECO), Department of Biology, University of Antwerp, B-2610 Wilrijk, Belgium

[32]Pasture Systems and Watershed Management Research Unit, USDA-ARS, University Park, PA, USA

[33]Virginia Commonwealth University, Department of Biology

[34]Terra Teaching and Research Center, University of Liège – Gembloux Agro-Bio Tech, 5030 Gembloux, Belgium.

[35]Center for Environmental Remote Sensing, Chiba University, Japan

[36]Department of Ecoscience, Aarhus University, Frederiksborgvej 399, Roskilde 4000, Denmark

[37]Department of Physical Geography and Ecosystem Science, Lund University, Sölvegatan 12, 223 62 Lund, Sweden

[38]Bioclimatology, University of Goettingen, 37077 Goettingen, Germany

[39]Department of Geography, McGill University, Montreal, Canada

[40]Department of Geography, The University of British Columbia, Vancouver, Canada

[41]Research Institute for Global Change, Japan Agency for Marine-Earth Science and Technology

[42]Finnish Meteorological Institute, Climate System Research Unit, P.O. Box 503, 00101 Helsinki, Finland

[43]Institute of Atmospheric and Earth System Research / Physics, University of Helsinki, Helsinki, Finland

[44]Institute of Landscape Ecology, University of Münster, Münster, Germany

[45]Environmental Science Division, Argonne National Laboratory, Lemont, IL, USA

[46]University of Chicago Consortium for Advanced Science & Engineering (CASE), Chicago, IL, USA

[47]Northwestern Argonne Institute of Science and Engineering, Evanston, IL, USA

[48]National Ecological Observatory Network, Battelle, 1685 38th Street, 80301 Boulder, CO, USA

[49]Department of Atmospheric and Oceanic Sciences, University of Wisconsin-Madison, 1225 W Dayton St, 53711 Madison, WI, USA

[50]Free University of Bolzano, Faculty of Agricultural, Environmental and Food Sciences - Universitätsplatz 1 - Piazza Università, 1 39100 Bozen-Bolzano

[51]Belle W. Baruch Institute of Coastal Ecology and Forest Science, Clemson University, Georgetown, SC, United States

[52]Forestry and Environmental Conservation Department, Clemson University, Clemson, SC, United States

[53]CEFE, Univ Montpellier, CNRS, EPHE, IRD, Montpellier, France

[54]Department of Forest Ecology and Management, Swedish University of Agricultural Sciences, Skogsmarksgränd 17, SE-901 83, Umeå, Sweden

[55]Hawkesbury Institute for the Environment, Western Sydney University, Penrith Australia 2751

[56]Departamento de Química e Física, Universidade Federal da Paraíba - Campus II, 58397-000 Areia, Paraíba, Brazil

[57]Plants and Ecosystems, Department of Biology, University of Antwerp, 2610 Wilrijk, Belgium

[58]University of Tuscia, Department for Innovation in Biological, Agro-food and Forest Systems (DIBAF)

[59]GFZ German Research Centre for Geosciences, Potsdam, Germany

[60]Forschungszentrum Jülich, Institute of Bio-and Geosciences: Agrosphere (IBG-3), 52428 Jülich, Germany

[61]Woodwell Climate Research Center: FALMOUTH, MA, US

[62]School of Science, Edith Cowan University, Australia

[63]University of Florida, Range Cattle Research and Education Center. 3401 Experiment Station, Ona, FL, USA 33865.

[64]Department of Agriculture Sciences, University of Sassari, Italy

[65]Department of Geosciences and Natural Resource Management, University of Copenhagen, Øster Voldgade 10, DK-1350 Copenhagen, Denmark
[66]Terrasystem srl
[67]Institute for Atmospheric and Earth System Research/Physics, Faculty of Science, University of Helsinki, Helsinki, 00014, Finland
[68]Institute for Atmospheric and Earth System Research/Forest Sciences, Faculty of Agriculture and Forestry, University of Helsinki, Helsinki, 00014, Finland
[69]UCLouvain - Earth and Life Institute (ELI) Croix du Sud, 2 bte L7.05.24 (de Serres B249) Ž013 1348 Louvain-la-Neuve
[70]Department of Methods and Models for Economics, Territory and Finance (MEMOTEF), Sapienza University of Rome, Via del Castro Laurenziano, 9, 00161, Rome,Italy
[71]School of Sustainable Engineering and the Built Environment, Arizona State University, Tempe, AZ, USA 85287-8704
[72]Center for Hydrologic Innovations, Arizona State University, Tempe, AZ, USA 85287-8704
[73]School of the Environment, The University of Queensland, 4072, Australia
[74]CSIRO, Space and Astronomy, Kensington, 6151, WA, Australia
[75]Instituto Tecnológico de Sonora, 5 de Febrero 818 Sur, Col. Centro, Cd. Obregon, Sonora, México, 85000
[76]School of life sciences, University of Qufu normal university, Qufu 273165, Shandong, China
[77]Institute of Applied Ecology, Chinese Academy of Sciences, Shenyang 110016, China
[78]Department Biology, San Diego State University, San Diego, CA 92182, USA

Correspondence: Jacob A Nelson (jnelson@bgc-jena.mpg.de) and Sophia Walther (sophia.walther@bgc-jena.mpg.de)

Abstract. Mapping in-situ eddy covariance measurements of terrestrial land-atmosphere fluxes to the globe is a key method for diagnosing the Earth system from a data-driven perspective. We describe the first global products (called X-BASE) from a newly implemented up-scaling framework, FLUXCOM-X, representing an advancement from the previous generation of FLUXCOM products in terms of flexibility and technical capabilities. The X-BASE products comprise of estimates of CO_2 net ecosystem exchange (NEE), gross primary productivity (GPP) as well as evapotranspiration (ET) and, for the first time, a novel fully data-driven global transpiration product (ET_T), at high spatial (0.05°) and temporal (hourly) resolution. X-BASE estimates the global NEE at -5.75 $\pm$ 0.33 $PgC \cdot yr^{-1}$ for the period 2001-2020, showing a much higher consistency with independent atmospheric carbon cycle constraints compared to the previous versions of FLUXCOM. The improvement of global NEE was likely only possible thanks to the international effort to increase the precision and consistency of eddy covariance collection and processing pipelines, as well as to the extension of the measurements to more site-years resulting in a wider coverage of bio-climatic conditions. However, X-BASE global net ecosystem exchange shows a very low inter-annual variability, which is common to state-of-the-art data-driven flux products and remains a scientific challenge. With 125 $\pm$ 2.1 $PgC \cdot yr^{-1}$ for the same period, X-BASE GPP is slightly higher than previous FLUXCOM estimates, mostly in temperate and boreal areas. X-BASE evapotranspiration amounts to 74.7x10^3 $\pm$ 0.9x10^3 km^3 globally for the years 2001-2020, but exceeds precipitation in many dry areas likely indicating overestimation in these regions. On average 57% of evapotranspiration are estimated to be transpiration, in good agreement with isotope-based approaches, but higher than estimates from many land surface models. Despite considerable improvements to the previous up-scaling products, many further opportunities for development exist. Pathways of exploration include methodological choices in the selection and processing of eddy-covariance and satellite observations, their ingestion into the framework, and the configuration of machine learning methods. For this,

20 the new FLUXCOM-X framework was specifically designed to have the necessary flexibility to experiment, diagnose, and converge to more accurate global flux estimates.

1 Introduction

Energy, water, and carbon exchange between terrestrial surfaces and the atmosphere are key components of the Earth system and impact ecosystems, ecosystem services, weather, climate, and water availability. The exchange (or flux) can be directly
25 observed using eddy covariance (EC) measurement systems (Baldocchi, 2019) which are installed on towers overlooking the ecosystem of interest. The EC stations typically represent an area of a few hundred square meters to a square kilometer. One key advantage of the EC methodology is the ability to provide near continuous measurements with some records now exceeding 20 years (Pastorello et al., 2020), allowing for examination of flux variations from the order of thirty minutes to decades. EC systems also provide a unique perspective on the magnitude, temporal variability, and environmental sensitivity
30 of ecosystem CO_2 uptake, water use, and local climate regulation (Baldocchi, 2019; Musavi et al., 2017; Bao et al., 2022). However, while many of the most pressing scientific knowledge gaps surrounding the delicate land carbon balance and the water cycle require spatially and temporally resolved flux patterns at continental to global scales, EC observations are confined to individual locations in space and limited periods in time (Kumar et al., 2016; Papale et al., 2015). Methodologies to transcend the gap between local and global scales are needed to ultimately support societal relevant activities of building greenhouse
35 gas monitoring systems, taking informed climate and land management actions, and verifying the effectiveness of mitigation strategies (Baldocchi and Penuelas, 2019; Bonan et al., 2011; Novick et al., 2022).

Coordinated and consolidated data collections from EC networks are invaluable for the mapping of in-situ fluxes to regional and global scales. For example, EC measurements aid both the parameterization (Huang et al., 2021) and the validation (Turner et al., 2006; Heinsch et al., 2006) of mechanistic models of ecosystem productivity and land surface processes. The latter
40 generate widely used reference data sets for terrestrial carbon cycle applications (Zhao and Running, 2010; Ukkola et al., 2022). A complementary approach to modeling terrestrial fluxes at continental and global scales is of empirical nature and links observations of explanatory variables at the EC stations, particularly meteorological and remote sensing data, to the EC fluxes via machine learning models. This up-scaling concept does not prescribe any mechanistic formulations and assumes that the EC observations cover all complexities of ecosystem functioning. Based on a trained machine learning model and globally
45 gridded input data of the explanatory variables, EC fluxes can be mapped to the global scale.

First implementations of this flux up-scaling concept emerged in the early 2000s. They focused on net ecosystem exchange of CO_2 (NEE) and utilized the growing EC networks in Europe (Papale and Valentini, 2003) and North America (Xiao et al., 2008). The release of the FLUXNET La Thuile Synthesis Dataset of harmonized EC data in 2007, as well as methodological improvements in the training of the machine learning models (Jung et al., 2009), led to the first global products of terrestrial
50 CO_2 and water fluxes at a monthly time step and in 0.5° grids in 2011 (Jung et al., 2011). While good agreement of flux estimates derived from complementary process-based models with the up-scaled global gross photosynthetic CO_2 uptake (gross primary productivity, GPP) and energy fluxes demonstrated the potential of the approach, important inconsistencies remained,

in particular regarding the globally integrated NEE and its year-to-year variability (Jung et al., 2020, 2019, 2011; Zscheischler et al., 2017). A critical component of data-driven methods, including the flux up-scaling methodologies described here, is understanding the related uncertainties. The multi-stage process of going from the actual measured values of high frequency (10-20 Hz) measurements of three-dimensional wind components, temperature, water vapor and CO2 concentration to the standard half-hourly, gap-filled, long-term data records from synthesis datasets such as FLUXNET have multiple associated potential biases and uncertainties. The well documented issues of gap-filling (Vekuri et al., 2023; Soloway et al., 2017; Papale et al., 2006), instrumentation errors (Zhang et al., 2023; Fratini et al., 2014; Vitale et al., 2020; Rannik et al., 2016), and energy balance non-closure (Mauder et al., 2020; Leuning et al., 2012; Stoy et al., 2013; McGloin et al., 2018; Franssen et al., 2010) will likely have an effect on the resulting gridded global datasets.

In an effort to better understand the uncertainties associated with mapping of EC fluxes to larger scales, the FLUXCOM inter-comparison initiative built an ensemble of flux estimates as a type of factorial experiment (Tramontana et al., 2016; Jung et al., 2019, 2020). The ensemble consisted of multiple machine learning algorithms, meteorological forcing data, and combinations of predictor variables resulting in 120 individual up-scaled estimates per flux. These were summarized in two overall ensemble configurations, which differed in the set of predictors and spatial-temporal resolution. Apart from creating a large ensemble, the FLUXCOM evaluation included a consistent site-level cross-validation analysis as well as cross-consistency checks with terrestrial flux estimates from independent approaches, such as complementary modeling concepts or observational surrogates. From a methodological point of view, the key lessons learned from FLUXCOM were that: (1) the overall approach seems to be primarily limited by the input information given to the machine learning algorithms rather than to the ability of the algorithm to extract the information; (2) the largest qualitative differences among flux products were related to the set of the predictor variables rather than to the choice of the machine learning method or meteorological forcing; (3) the cross-consistency checks with global independent data are essential for supplementing site-level cross-validation; and (4) the largest qualitative discrepancy with independent data was a very high (strongly negative) tropical NEE that was shared among all ensemble members.

Next to the systematic inter-comparisons in FLUXCOM, the empirical up-scaling concept has been implemented for a series of regional and global scale applications, each of them adopting disparate and individual methodological choices (e.g. Ichii et al., 2017; Yao et al., 2018; Joiner and Yoshida, 2020; Virkkala et al., 2021; Dannenberg et al., 2023; Burton et al., 2023; Zhu et al., 2024). These potentially important choices relate to data treatment (quality control, gap-filling, processing pathways), ingestion (sampling, as well as matching EC and space-born observations), and methodological configurations (machine learning methods and their training configuration, choice of predictor variables, resolution). The disparity of the set-ups and implementations of the empirical up-scaling approach impedes any direct comparisons among products and valid conclusions as to where potential differences originate from. Hence, flexibility to explore the large methodological space, as well as the ability to diagnose and evaluate global products in parallel to site-level cross-validation, are required to understand the importance of individual methodological choices and to make progress in empirical up-scaling of EC fluxes.

We are developing a modeling framework that allows experimenting with many of these methodological choices. We coin this extended up-scaling environment FLUXCOM-X. Compared to the FLUXCOM inter-comparison initiative and the prod-

ucts produced therein, it follows the same overall principles. The key innovation of FLUXCOM-X is that it represents a flexibly adjustable up-scaling environment to systematically explore different methodological avenues. Lessons learned from FLUXCOM and other up-scaling exercises further imply striving for enhancing the information content of the training data with aspects related to coverage and quality of EC measurements as well as complementarity, completeness, and quality of predictor variables. The flexibility of the way FLUXCOM-X is implemented will considerably reduce the latency with which innovations in the related fields of machine learning and spacebased Earth observations as well as novel EC data can find their way to empirical flux up-scaling. This in turn allows faster progress towards more accurate and fit-for-the-purpose global biogenic flux estimates. Here, we introduce and evaluate the initial "basic" set of products from this flexible framework, which we refer to as FLUXCOM-X-BASE products (or X-BASE for short, see Appendix A for an overview on the naming conventions).

X-BASE products were comparably generated to the original FLUXCOM ensemble using qualitatively similar predictor variables, i.e. remotely sensed vegetation indices and land surface temperatures from the Moderate Resolution Imaging Spectroradiometer (MODIS) along with meteorological variables. In contrast to FLUXCOM, the remotely sensed and the meteorological predictors are combined in the X-BASE products, and the subdaily variability is resolved. We furthermore made efforts to provide more and improved information to the machine learning models by enhancing coverage and quality of the training data, and by further developing the processing of satellite predictor variables (Walther and Besnard et al., 2022). In this manuscript, we show results for X-BASE NEE, GPP, evapotranspiration (ET), and for the first time transpiration (ET_T), for the period 2001-2020 at 0.05° spatial and hourly temporal resolution. We are focusing here on the evaluation and cross-consistency checks of X-BASE with previous FLUXCOM products and independent data streams. Our specific objectives are:

1. to describe the production of X-BASE products;
2. to evaluate the X-BASE setup using site-level cross-validation;
3. to assess qualitative differences of global patterns compared to previous FLUXCOM products with reference to independent flux estimates where possible; and
4. to synthesize lessons learned from this basic exercise to guide future FLUXCOM-X developments.

X-BASE products are freely available and serve as a baseline for future FLUXCOM-X developments (see data availability statement). Any future product releases originating from FLUXCOM-X will follow the naming convention X-[specific name].

2 Data and Methods

The following section gives an overview on the essential methodological implementations and data choices adopted in the generation of X-BASE products.

2.1 Eddy Covariance Data

Eddy covariance data consisted of 294 sites from around the world though skewed towards higher representation from temperate forests from North America and Europe. All EC data were collected, processed, analyzed for quality by the station teams, before being processed using state-of-the-art approaches in the ONEFLUX data processing pipeline (Pastorello et al., 2020). ONEFLUX provides consistent quality checks, gap-filling, and carbon flux partitioning. The data included was collected between 2001-2020 and available with a CC BY 4.0 license. Based on this criterion, data for each site came from one of five different sources based on most recent availability: FLUXNET 2015 (Pastorello et al., 2020), ICOS Drought 2018 (Team and Centre, 2020), ICOS Warm Winter 2020 (Team and Centre, 2022), or the most recent Ameriflux or ICOS release as of December 2022. Table 1 lists all sites included as well as the associated digital object identifier specific to the associated release.

Table 1: **Citation data for the 294 sites used in the X-BASE products.**

AR-SLu (Garcia et al., 2016)	AR-TF1 (Kutzbach, 2021)	AR-Vir (Posse et al., 2016)	AT-Neu (Wohlfahrt et al., 2016)	AU-ASM (Cleverly and Eamus, 2016b)	AU-Ade (Beringer and Hutley, 2016c)
AU-Cpr (Meyer et al., 2016)	AU-Cum (Pendall and Griebel, 2016)	AU-DaP (Beringer and Hutley, 2016b)	AU-DaS (Beringer and Hutley, 2016f)	AU-Dry (Beringer and Hutley, 2016e)	AU-Emr (Schroder et al., 2016)
AU-Fog (Beringer and Hutley, 2016a)	AU-Gin (Macfarlane et al., 2016)	AU-RDF (Beringer and Hutley, 2016d)	AU-Rob (Liddell, 2016)	AU-TTE (Cleverly and Eamus, 2016a)	AU-Tum (Woodgate et al., 2016)
AU-Wac (Beringer et al., 2016b)	AU-Whr (Beringer et al., 2016a)	AU-Wom (Arndt et al., 2016)	AU-Ync (Beringer and Walker, 2016)	BE-Bra (Team and Centre, 2022)	BE-Dor (Team and Centre, 2022)
BE-Lcr (RI, 2021)	BE-Lon (Team and Centre, 2022)	BE-Maa (Team and Centre, 2022)	BE-Vie (Team and Centre, 2022)	BR-Npw (Vourlitis et al., 2022)	BR-Sa1 (Saleska, 2016)
BR-Sa3 (Goulden, 2016d)	CA-Cbo (Staebler, 2022)	CA-DB2 (Knox, 2022)	CA-DBB (Christen and Knox, 2022)	CA-ER1 (Wagner-Riddle, 2021)	CA-Gro (McCaughey, 2016)
CA-LP1 (Black, 2021)	CA-Man (Amiro, 2016b)	CA-NS2 (Goulden, 2016a)	CA-NS3 (Goulden, 2016b)	CA-NS4 (Goulden, 2016c)	CA-NS5 (Goulden, 2016g)
CA-NS6 (Goulden, 2016e)	CA-NS7 (Goulden, 2016f)	CA-Oas (Black, 2016b)	CA-Obs (Black, 2016a)	CA-Qfo (Margolis, 2016)	CA-SF1 (Amiro, 2016c)

Table 1: **Citation data for the 294 sites used in the X-BASE products.**

CA-SF2 (Amiro, 2016a)	CA-SF3 (Amiro, 2016d)	CA-TP1 (Arain, 2016b)	CA-TP2 (Arain, 2016a)	CA-TP3 (Arain, 2022b)	CA-TP4 (Arain, 2016c)
CA-TPD (Arain, 2022a)	CG-Tch (Nouvellon, 2016)	CH-Aws (Team and Centre, 2022)	CH-Cha (Team and Centre, 2022)	CH-Dav (Team and Centre, 2022)	CH-Fru (Team and Centre, 2022)
CH-Lae (Team and Centre, 2022)	CH-Oe1 (Ammann, 2016)	CH-Oe2 (Team and Centre, 2022)	CN-Cha (Zhang and Han, 2016)	CN-Cng (Dong, 2016)	CN-Dan (Shi et al., 2016)
CN-Din (Zhou and Yan, 2016)	CN-Du2 (Chen, 2016k)	CN-Du3 (Shao, 2016b)	CN-HaM (Tang et al., 2016)	CN-Qia (Wang and Fu, 2016)	CN-Sw2 (Shao, 2016a)
CZ-BK1 (Team and Centre, 2022)	CZ-BK2 (Sigut et al., 2016)	CZ-KrP (Team and Centre, 2022)	CZ-Lnz (Team and Centre, 2022)	CZ-RAJ (Team and Centre, 2022)	CZ-Stn (Team and Centre, 2022)
CZ-wet (Team and Centre, 2022)	DE-Akm (Team and Centre, 2022)	DE-Geb (Team and Centre, 2022)	DE-Gri (Team and Centre, 2022)	DE-Hai (Team and Centre, 2022)	DE-HoH (Team and Centre, 2022)
DE-Hte (Team and Centre, 2020)	DE-Hzd (Team and Centre, 2022)	DE-Kli (Team and Centre, 2022)	DE-Lkb (Lindauer et al., 2016)	DE-Lnf (Knohl et al., 2016)	DE-Obe (Team and Centre, 2022)
DE-RuR (RI, 2022)	DE-RuS (Team and Centre, 2022)	DE-RuW (Team and Centre, 2022)	DE-Seh (Schneider and Schmidt, 2016)	DE-SfN (Klatt et al., 2016)	DE-Spw (Bernhofer et al., 2016)
DE-Tha (Team and Centre, 2022)	DE-Zrk (Sachs et al., 2016)	DK-Eng (Pilegaard and Ibrom, 2016)	DK-Fou (Olesen, 2016)	DK-Gds (RI, 2022)	DK-Sor (Team and Centre, 2022)
ES-Abr (Team and Centre, 2022)	ES-Agu (Team and Centre, 2022)	ES-Amo (Poveda et al., 2016)	ES-Cnd (Team and Centre, 2022)	ES-LJu (Team and Centre, 2022)	ES-LM1 (Team and Centre, 2022)
ES-LM2 (Team and Centre, 2022)	ES-LgS (Reverter et al., 2016b)	ES-Ln2 (Reverter et al., 2016a)	FI-Hyy (Team and Centre, 2022)	FI-Jok (Lohila et al., 2016)	FI-Ken (Team and Centre, 2022)
FI-Let (Team and Centre, 2022)	FI-Lom (Aurela et al., 2016a)	FI-Qvd (Team and Centre, 2022)	FI-Sii (Team and Centre, 2022)	FI-Sod (Aurela et al., 2016b)	FI-Var (RI, 2022)
FR-Aur (Team and Centre, 2022)	FR-Bil (Team and Centre, 2022)	FR-EM2 (RI, 2022)	FR-FBn (Team and Centre, 2022)	FR-Fon (Team and Centre, 2022)	FR-Gri (Team and Centre, 2022)
FR-Hes (Team and Centre, 2022)	FR-LBr (Berbigier and Loustau, 2016)	FR-LGt (RI, 2022)	FR-Lam (Team and Centre, 2022)	FR-Pue (Ourcival, 2016)	FR-Tou (RI, 2022)

Table 1: **Citation data for the 294 sites used in the X-BASE products.**

GF-Guy (Team and Centre, 2022)	GH-Ank (Valentini et al., 2016b)	GL-Dsk (RI, 2022)	GL-NuF (Hansen, 2016)	GL-ZaF (Lund et al., 2016b)	GL-ZaH (Lund et al., 2016a)
IE-Cra (Team and Centre, 2022)	IL-Yat (Team and Centre, 2022)	IT-BCi (Team and Centre, 2022)	IT-BFt (RI, 2022)	IT-CA1 (Sabbatini et al., 2016c)	IT-CA2 (Sabbatini et al., 2016a)
IT-CA3 (Sabbatini et al., 2016b)	IT-Col (Matteucci, 2016)	IT-Cp2 (Team and Centre, 2022)	IT-Cpz (Valentini et al., 2016a)	IT-Isp (Gruening et al., 2016b)	IT-La2 (Cescatti et al., 2016)
IT-Lav (Team and Centre, 2022)	IT-Lsn (RI, 2022)	IT-MBo (Team and Centre, 2022)	IT-Noe (Spano et al., 2016)	IT-PT1 (Manca and Goded, 2016)	IT-Ren (Team and Centre, 2022)
IT-Ro1 (Valentini et al., 2016c)	IT-Ro2 (Papale et al., 2016)	IT-SR2 (Team and Centre, 2022)	IT-SRo (Gruening et al., 2016a)	IT-Tor (Team and Centre, 2022)	JP-MBF (Kotani, 2016b)
JP-SMF (Kotani, 2016a)	MX-Tes (Yepez and Garatuza, 2021)	MY-PSO (Kosugi and Takanashi, 2016)	NL-Hor (Dolman et al., 2016a)	NL-Loo (Team and Centre, 2020)	PA-SPn (Wolf et al., 2016b)
PA-SPs (Wolf et al., 2016a)	PE-QFR (Griffis and Roman, 2021)	RU-Che (Merbold et al., 2016)	RU-Cok (Dolman et al., 2016b)	RU-Fy2 (Team and Centre, 2022)	RU-Fyo (Team and Centre, 2022)
RU-Ha1 (Belelli et al., 2016)	SD-Dem (Ardö et al., 2016)	SE-Deg (Team and Centre, 2022)	SE-Htm (Team and Centre, 2022)	SE-Lnn (Team and Centre, 2020)	SE-Nor (Team and Centre, 2022)
SE-Ros (Team and Centre, 2022)	SE-Svb (Team and Centre, 2022)	SJ-Adv (Christensen, 2016)	SJ-Blv (Boike et al., 2016)	SN-Dhr (Tagesson et al., 2016)	US-A32 (Billesbach et al., 2022)
US-AR1 (Billesbach et al., 2016b)	US-AR2 (Billesbach et al., 2016a)	US-ARM (Biraud et al., 2022)	US-ARb (Torn, 2016b)	US-ARc (Torn, 2016a)	US-Atq (Zona and Oechel, 2016a)
US-BZB (Euskirchen, 2022b)	US-BZF (Euskirchen, 2022c)	US-BZS (Euskirchen, 2022d)	US-BZo (Euskirchen, 2022a)	US-Bi1 (Rey-Sanchez et al., 2022b)	US-Bi2 (Rey-Sanchez et al., 2022a)
US-Blo (Goldstein, 2016)	US-CF1 (Huggins, 2021)	US-CF2 (Huggins, 2022c)	US-CF3 (Huggins, 2022a)	US-CF4 (Huggins, 2022b)	US-CRT (Chen and Chu, 2016b)
US-CS1 (Desai, 2022a)	US-CS2 (Desai, 2022c)	US-CS3 (Desai, 2022d)	US-CS4 (Desai, 2022b)	US-Cop (Bowling, 2016)	US-EDN (Oikawa, 2021)

Table 1: **Citation data for the 294 sites used in the X-BASE products.**

US-GBT (Massman, 2016)	US-GLE (Massman, 2022)	US-Goo (Meyers, 2016b)	US-HB1 (Forsythe et al., 2021)	US-HWB (Goslee, 2022)	US-Ha1 (Munger, 2016)
US-Hn3 (Liu et al., 2022)	US-Ho2 (Hollinger, 2022)	US-IB2 (Matamala, 2016)	US-ICs (Euskirchen et al., 2022a)	US-ICt (Euskirchen et al., 2022b)	US-Ivo (Zona and Oechel, 2016b)
US-Jo2 (Vivoni and Perez-Ruiz, 2022)	US-KFS (Brunsell, 2022a)	US-KLS (Brunsell, 2022b)	US-KS1 (Drake and Hinkle, 2016a)	US-KS2 (Drake and Hinkle, 2016b)	US-KS3 (Hinkle, 2022)
US-LWW (Meyers, 2016a)	US-Lin (Fares, 2016)	US-Los (Desai, 2016c)	US-MMS (Novick and Phillips, 2022)	US-MOz (Wood and Gu, 2022)	US-Me1 (Law, 2016c)
US-Me2 (Law, 2022)	US-Me3 (Law, 2016a)	US-Me4 (Law, 2016e)	US-Me5 (Law, 2016d)	US-Me6 (Law, 2016b)	US-Mpj (Litvak, 2021)
US-Myb (Sturtevant et al., 2016)	US-NGB (Torn and Dengel, 2021)	US-NR1 (Blanken et al., 2022)	US-Ne1 (Suyker, 2022)	US-Ne2 (Suyker, 2016b)	US-Ne3 (Suyker, 2016a)
US-ONA (Silveira, 2021)	US-ORv (Bohrer, 2021)	US-OWC (Bohrer and Kerns, 2022)	US-Oho (Chen et al., 2016)	US-PFa (Desai, 2016d)	US-Prr (Kobayashi and Suzuki, 2016)
US-Rms (Flerchinger, 2022c)	US-Ro1 (Baker et al., 2022)	US-Ro4 (Baker and Griffis, 2022a)	US-Ro5 (Baker and Griffis, 2021)	US-Ro6 (Baker and Griffis, 2022b)	US-Rwe (Flerchinger and Reba, 2022)
US-Rwf (Flerchinger, 2022a)	US-Rws (Flerchinger, 2022b)	US-SRC (Kurc, 2022)	US-SRG (Scott, 2016a)	US-SRM (Scott, 2016b)	US-Sne (Shortt et al., 2022)
US-Snf (Kusak et al., 2022)	US-Sta (Ewers and Pendall, 2016)	US-Syv (Desai, 2016b)	US-Ton (Baldocchi and Ma, 2016)	US-Tw1 (Valach et al., 2021)	US-Tw2 (Sturtevant et al., 2022)
US-Tw3 (Chamberlain et al., 2022)	US-Tw4 (Sanchez et al., 2016)	US-Tw5 (Valach et al., 2022)	US-Twt (Baldocchi, 2016)	US-UM3 (Bohrer, 2022)	US-UMB (Gough et al., 2016)

Table 1: **Citation data for the 294 sites used in the X-BASE products.**

US-UMd (Gough et al., 2022)	US-Var (Baldocchi et al., 2016)	US-WCr (Desai, 2016a)	US-WPT (Chen and Chu, 2016a)	US-Whs (Scott, 2016d)	US-Wi0 (Chen, 2016g)
US-Wi1 (Chen, 2016e)	US-Wi2 (Chen, 2016j)	US-Wi3 (Chen, 2016b)	US-Wi4 (Chen, 2016d)	US-Wi5 (Chen, 2016a)	US-Wi6 (Chen, 2016h)
US-Wi7 (Chen, 2016i)	US-Wi8 (Chen, 2016c)	US-Wi9 (Chen, 2016f)	US-Wjs (Litvak, 2022)	US-Wkg (Scott, 2016c)	US-xBR (Network), 2022)

Meteorological data measured at each site consisted of incoming shortwave radiation, air temperature and vapor pressure deficit, of which all data were gap-filled using the Marginal Distribution Sampling method (Reichstein et al., 2005), as well as the computed potential shortwave incoming radiation (top of atmosphere theoretical maximum radiation) for every hour.

130   Carbon dioxide flux data consisted of gap-filled net ecosystem exchange (NEE, variable ustar threshold 50th percentile i.e., NEE_VUT_50) and the corresponding gross primary productivity (GPP, nighttime partitioning method after Reichstein et al. (2005)). Water flux data consisted of evapotranspiration (ET, no energy balance correction) which was converted from the latent energy and transpiration estimates based on the Transpiration Estimation Algorithm (TEA, Nelson et al. (2018); Nelson (2021)). The TEA algorithm estimates transpiration based on the relationship between GPP and ET under conditions where

135   surface and soil evaporation are expected to be minimal and accounting for residual non-transpiration evaporation. Note that estimates of GPP and transpiration are not direct measurements but instead based on statistical relationships localized to each station and time period and thus contain their own assumption and uncertainties. All data were aggregated to a common hourly time resolution, an overview of which can be found in Table 2.

Table 2: **Fluxes to be predicted and predictor variables used in X-BASE.** The units of the fluxes correspond to the native hourly resolution. Upon temporal aggregation as in some analyses in the presented results, the units may change.

predicted fluxes		
NEE	$\mu mol\, CO_2 \cdot m^{-2} \cdot s^{-1}$	net ecosystem exchange
GPP	$\mu mol\, CO_2 \cdot m^{-2} \cdot s^{-1}$	gross primary productivity
ET	$mm \cdot hr^{-1}$	evapotranspiration
ET_T	$mm \cdot hr^{-1}$	transpiration

predictor variables	
air temperature	$^{\circ}C$

predictor variables	
vapor pressure deficit	hPa
incoming shortwave radiation	$W \cdot m^{-2}$
potential incoming shortwave radiation	$W \cdot m^{-2}$
derivative of daily pot. incoming shortwave radiation	$W \cdot m^{-2} \cdot d^{-1}$
derivative of hourly pot. incoming shortwave radiation	$W \cdot m^{-2} \cdot hr^{-1}$
daytime land surface temperature from MODIS TERRA	Kelvin
nighttime land surface temperature from MODIS TERRA	Kelvin
enhanced vegetation index	-
near-infrared reflectance of vegetation	-
normalized difference water index	-
plant functional type	-

Data from the EC dataset that ultimately were used for training the models varied between ~12-14 million site-hours depending on the target variable (i.e. GPP, NEE, ET, or ET_T). Training of the machine learning algorithms was only conducted on hours where all input variables passed quality control. The quality control procedure consisted of two levels, with the first being each hour must have at least one value of good quality measured or gap-filled with confidence (i.e. at least one half hour was either 0 or 1 based on the OneFLUX _QC flags). Second, a set of consistency tests were performed on each used variable to check the consistency both among variables and across sites. As the consistency flags were based on daily aggregates of the meteorological and flux data, entire days were removed if the test indicated inconsistencies among related variables. The consistency flag also checked the relationship between variables across sites, ensuring that the relationships found across the data are coherent. A detailed explanation of these consistency flags can be found in Jung et al. (2024).

2.2 Global Meteorology

For the generation of global flux maps we used hourly meteorological data from ERA5 global reanalysis products at 0.25° (Hersbach et al., 2020). Variables included air temperature at 2m height, incoming shortwave radiation at the surface, as well as vapour pressure deficit (computed from relative humidity, air temperature, and surface pressure). Units were converted to correspond to the site level measurements which were used for training the machine learning model, and the data were re-gridded to a 0.05° resolution using bilinear interpolation for every hour.

2.3 Satellite Earth Observation

The X-BASE products are based on measurements of the MODerate Imaging Spectroradiometer (MODIS) of surface reflectance and land surface temperature from collection 006 at daily resolution. Missing records were gap-filled consistently

in both the average time series per EC station and in the global gridded data following the procedures of the FluxnetEO data version 2 (Walther and Besnard et al., 2022; Walther, 2023).

2.3.1 Spectral vegetation indices

At site level we used surface reflectance in the first seven MODIS spectral bands from the MCD43A4 c006 reflectance data set (500 m and daily, where each daily value is inverted from all valid observations within a 16-day window, Schaaf and Wang (2015b)). The spectral vegetation indices computed from the reflectance data were the enhanced vegetation index (EVI, Huete et al. (2002)), the spectral reflectance of vegetation in the near-infrared (NIRv, Badgley et al. (2017)), and the normalized difference water index (NDWI) with MODIS band 7 as reference (Gao, 1996). We followed the procedure of the FluxnetEO data sets version 2 (Walther and Besnard et al., 2022) for data acquisition from Google Earth Engine for all pixels in a cutout of 4x4 km^2 around each EC station, as well as for quality checks in terms of cloud, snow, and land cover, index values outside the defined ranges, and outliers. An iterative approach then determined both, the strictness of the inversion quality of the bidirectional reflectance distribution function (BRDF, based on the MCD43A2 data, Schaaf and Wang (2015a)) and the set of pixels in a cutout that shall represent a given EC station. Appendix B1 outlines all technical details of the dynamic procedure.

Global data of BRDF-corrected surface reflectance stem from the MCD43C4 c006 data (Schaaf and Wang, 2015b), available in a climate modelling grid of 0.05° with the same temporal sampling and subject to the same removal of snow and water pixels and outlier values like at site level. The BRDF quality control of the global data followed the same dynamic approach (see Appendix B1), which maximized data availability especially in tropical regions.

2.3.2 Land surface temperature

Satellite observations of land surface temperature (LST) were based on the MODIS c006 TERRA observations which are available every day at 1 km resolution (Wan et al., 2015). We selected the 1 km^2 pixel containing a specific tower and treated the two MODIS LST data streams as independent predictor variables which represent clear-sky LST at a specific time of the day (namely around 10.30 AM and PM local time). Quality checks and gap-filling followed the procedure described in FluxnetEO version 2 (Walther and Besnard et al., 2022).

For the global spatialization of the flux estimates we relied on climate modelling grid LST from the MODIS TERRA data sets (Wan et al., 2015) and apply consistent quality control and imputation of missing values like at site-level.

2.3.3 Land cover

Land cover information used the IGBP global vegetation classification. Site level classification was as reported by the principal investigators. Global data were based on the yearly-resolved MODIS MCD12C1 c006 product (Friedl and Sulla-Menashe, 2015). In order to ease the transition between site and global land cover classifications, an intermediate classification scheme was utilized which translated each classification into characteristics (e.g. trees, crops, needleleaf, deciduous, etc...) based on

whether the classification has (value=1.0), might have (value=0.5), does not have (value=0.0) a specific feature, or is unknown (value=-1.0). A full description of this intermediate classification system can be found in Appendix B2.

2.4 Machine Learning Method

All X-BASE products are based on gradient boosted regression trees using the XGBoost library (Chen and Guestrin, 2016). XGBoost is known as a robust algorithm that is able to handle a variety of variable types (numeric, boolean, categorical). Training was conducted using a two-thirds training sub-sampling ratio and a 0.05 learning rate. Hyperparameters were chosen based on preliminary testing to predict eddy covariance data, and a full list of hyperparameters can be found in Appendix B3. Boosting was stopped when no model improvement (based on mean squared error of validation data) was observed for ten consecutive rounds, and the best performing model was stored to generate predictions. In all cases, the model reached the stopping criteria relatively quickly, with the final number of boosting rounds between 80-230, depending on the flux.

2.5 Cross-validation

All cross-validation was performed using a ten-fold, leave-site-fold-out scheme, where each fold was constructed by randomly assigning each site to a fold. For each round of cross-validation, eight folds were used for training, one for validation and the remaining one as the test fold for which the actual predictions were made. The leave-site-fold-out scheme ensures that no data from the sites in the test fold were ever seen by the algorithm during training, and in turn iterated such that each site was in the test set once. As eddy covariance sites are sometimes clustered in the same location (e.g. as different treatments) and can therefore be both physically closely located and not truly independent, sites are assigned to the same fold if they are less than 0.05° apart to reduce over-fitting. We evaluate the accuracy of the cross-validation models by computing the Nash-Sutcliffe modeling efficiency (NSE, Nash and Sutcliffe (1970)), where a negative NSE indicates a model accuracy that is worse than a mean prediction, while a value close to one indicates high model accuracy. We compute the NSE for each site and for a range of temporal scales from hourly to inter-annual.

2.6 Up-scaling

The final step to train a model to use in the final global prediction step was identical to the training in the cross-validation, with the exception that, because no test fold was required, we used nine of the ten folds for the training and validation was done on the remaining fold. The final trained models (one trained model for each target flux) were then used to predict fluxes at the global scales using the associated globally gridded input variables that correspond to those used at site level, as outlined in Table 2.

2.7 Previous FLUXCOM and independent global flux estimates

We compare X-BASE with up-scaling results from FLUXCOM (Jung et al., 2019, 2020). As mentioned earlier, FLUXCOM comprised an ensemble of up-scaling experiments that differed in the choice of machine learning method, meteorological forc-

ing data, and which were summarized in two groups of set-ups that shared the same predictor variables and spatiotemporal resolution: The "remote-sensing-only" set-up (RS) mostly used spaceborne observations of MODIS as explanatory variables and produced flux estimates every 8 days at 0.083° resolution, while the 'remote-sensing plus meteorology set-up' (RS+METEO) produced daily flux estimates at half degree resolution from meteorological predictor variables and an average seasonal cycle of satellite observations (Tramontana et al., 2016; Jung et al., 2019, 2020). Comparisons to FLUXCOM RS+METEO datasets always refer to the ensemble over multiple machine learning methods for all realizations driven by the ERA5 meteorology (Hersbach et al., 2020). RS+METEO uses average seasonal cycles of MODIS c005 observations. For the FLUXCOM RS setup we use the ensemble over all machine learning methods. Please note that both the previous RS runs and the X-BASE runs presented here are driven by data from MODIS c006, but the processing has changed in some aspects such as quality control and gap-filling. For clarification, an overview on FLUXCOM(-X) naming conventions is given in Appendix A.

For evaluating X-BASE NEE globally, in particular its seasonal cycle and for different regions, we used two different atmospheric inversion model products: the Orbiting Carbon Observatory-2 (OCO-2) v10 model intercomparison project (Byrne et al., 2023) and the CarboScope inversion (Rödenbeck et al., 2018) version s99oc_v2022 (Roedenbeck and Heimann, 2022). Estimates from the OCO-2 came from the the LNLGIS experiment which combines satellite-based column-averaged CO_2 (XCO2) retrievals and in-situ CO_2 measurements as observational constraints in the assimilation, and consists of 13 different ensemble members covering the period 2015-2020 with a monthly frequency and 1° spatial resolution (https://gml.noaa.gov/ccgg/OCO2_v10mip/index.php). The CarboScope product consisted of a single inversion output at the same spatial resolution as OCO-2, but a longer temporal period from 2001 to 2020. In each case, as the inversion products estimate net biome exchange, we subtracted from the inversions data fire emissions as estimated by the Global Fire Emissions Database, Version 4.1 (Randerson et al., 2017).

We compared temporal patterns of X-BASE GPP with the patterns in global retrievals of sun-induced chlorophyll fluorescence (SIF) from the Sentinel-5P TROPOMI instrument (Köhler et al., 2018), which under most conditions approximate the variability in GPP. For the comparison we used estimates of daily mean SIF applying a correction factor to instantaneous observations (Zhang et al., 2018) and averaged both X-BASE GPP and TROPOMI SIF to a temporal resolution of 16 days and 0.5° spatial grids for the common period 04/2018-12/2020.

X-BASE ET and ET_T were cross-compared with transpiration estimates from the Global Land Evaporation Amsterdam Model (GLEAM) v3.6a (Martens et al., 2017; Miralles et al., 2011). GLEAM also utilizes satellite and reanalysis data sets but in a more physically constrained way, relying on semi-empirical models such as the Priestley and Taylor (Priestley and Taylor, 1972) and Gash models (Gash, 1979). Further comparisons were made to precipitation data from GPCC (Schneider et al., 2022).

2.8 Units across scales and conversion

Given the broad range of spatial and temporal scales reported here, we utilized different units depending on each use case. All base measurements and predictions are at hourly timescale and in units of $\mu mol\,CO_2 \cdot m^{-2} \cdot s^{-1}$ for carbon fluxes and $mm \cdot hr^{-1}$ for water fluxes (as reported in Table 2). In the case of carbon fluxes, all timescales which are not sub-daily are

reported in grams carbon per unit time and area. Globally integrated values are reported in Pg carbon or km^2 water and are aggregated using a common land area estimate per grid cell.

3 Results

3.1 Cross-validation and data space

One important innovation in FLUXCOM-X compared to the previous FLUXCOM ensemble was the training data base, which was larger due to an incease in both number of sites and years. Furthermore, the EC methodology has changed considerably in many aspects ranging from collection and processing to quality filtering in the last 15 years. We show here one illustrative example of the changes in the environmental space that is represented in the training samples for daily NEE: between daily VPD and daily incoming shortwave radiation the distribution of training samples was considerably broader in X-BASE compared to the RS+METEO ensemble (Fig. 1). Furthermore, the number of unique sites contributing to a certain VPD-radiation bin has increased (Fig. C1), i.e. the number of ecosystems sampled in each climatic condition has also increased. The increases were seen particularly at the margins of the distribution, i.e. for days with high VPD along the full radiation spectrum, and vice versa for days with high radiation conditions along the full VPD spectrum. Remarkably, the number of sites contributing training samples for high VPD *and* high radiation were observed much more frequently (Fig. 1) and at more sites (Fig. C1) compared to RS+METEO - providing more and more varied information for dry conditions. Overall for NEE, the number of sampled site-days increased over three-fold (552878 to 183216 for X-BASE and RS+METEO respectively), note however that X-BASE is modeled at hourly instead of daily resolution and thus the number of sampled site-days should not be considered a metric of how well the feature space is sampled.

The results from the ten-fold cross validation showed an overall high performance with most fluxes and scales of variability having an NSE above 0.6 (Fig. 2). In terms of scales of variability across all fluxes, the monthly mean diel cycle ("diel") and the daily median seasonal cycle ("seasonal") were very regular patterns that the trained models reproduced best. Also, among-site changes ("spatial", except for NEE) and monthly aggregated fluxes ("monthly") were reliably predicted. Deviations from the median daily seasonality ("anom") were only moderately reliable with NSE between 0.25 and 0.5. The XGBoost models did not succeed in accurately reproducing inter-annual changes ("i.a.v.") of all fluxes and between-site patterns in NEE. Consistently across all scales, the net fluxes which are directly calculated (i.e., ET and even more so NEE) showed lower performance than their respective modelled gross fluxes (i.e., GPP and ET_T). Note that the cross validation results from Fig. 2 cannot be quantitatively compared to previous cross validation results in FLUXCOM as the training data are not the same. However, qualitatively the accuracy gradient among fluxes, as well as along scales of variability, corresponded to patterns identified in FLUXCOM and in comparable empirical modeling activities (Jung et al., 2011; Tramontana et al., 2016; Virkkala et al., 2021; Dannenberg et al., 2023).
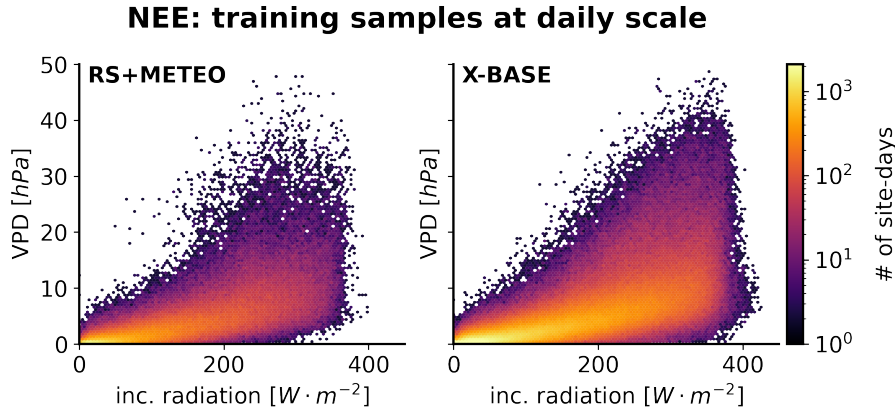
Figure 1. Cross-validation sampling in meteorological space: Number of site-days contributing to sampling for NEE for the previous FLUXCOM RS+METEO ensemble (left) compared to the sampling of FLUXCOM-X-BASE (right) in environmental space of daily aggregated incoming shortwave radiation and VPD. Color corresponds to number of site days per bin in log scale. Only bins with at least twenty site-days are shown.
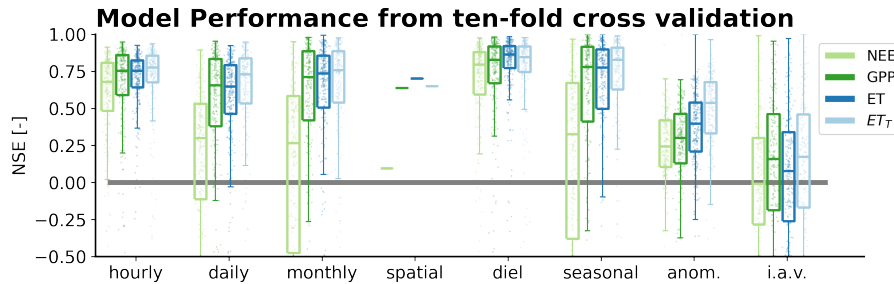
Figure 2. FLUXCOM-X-BASE site-level accuracy of predicted fluxes in ten-fold leave-site-fold-out cross-validation in terms of NSE computed per site for a range of scales of variability. Scales of variability include the hourly timescale ("hourly"), daily ("daily") and monthly ("monthly") aggregated fluxes, as well as between-site changes ("spatial"), monthly mean diel cycle ("diel"), daily median seasonal cycle ("seasonal"), deviations from the median daily seasonality ("anom."), and inter-annual variability ("i.a.v."). Boxes denote the range from the 25th to the 75th percentile of sites, whiskers extend 1.5 times the interquartile range from the 25th and 75th percentile of NSE across sites.
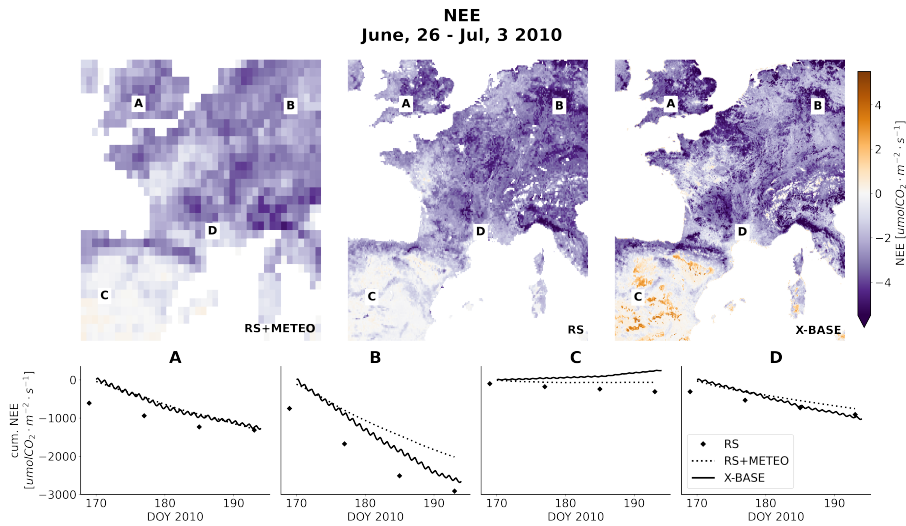
Figure 3. Resolution improvements for the X-BASE products compared to RS and RS+METEO: Average NEE for an 8-day period in Europe in 2010 as estimated from the RS, RS+METEO and X-BASE set-ups (top panel), as well as snapshots of temporal trajectories of NEE in pixels closest to selected EC station locations (A:UK-Tad, B: DE-Hai, C: ES-LM1, D: FR-Pue). Negative values of NEE denote a CO_2 flux from the atmosphere to the land.

3.2 Global flux estimates

One asset of FLUXCOM-X is flexibility in the spatiotemporal resolution of the flux estimates. We are producing X-BASE products at 0.05° spatial and hourly temporal resolution globally. Figure 3 illustrates the increase in spatial and temporal detail in X-BASE compared to RS (0.083°, 8-daily) and RS+METEO (0.5°, daily) using the example of NEE.

285 3.2.1 Net Ecosystem Exchange (NEE)

The X-BASE product estimates the global terrestrial NEE to be -5.75 ± 0.33 $PgC \cdot yr^{-1}$ (2001-2020), with hotspots of strong CO_2 flux into the ecosystems in the tropical regions, and temperate regions of North America and Europe (Fig. 4). In contrast to both RS and RS+METEO, India and some regions in central Sahel show prominent patterns of a mean CO_2 flux from the ecosystems to the atmosphere in X-BASE, corresponding mostly to crop designated areas (Fig. C2). However, X-BASE global
290 terrestrial NEE (-5.63 $PgC \cdot yr^{-1}$) agrees well with the inversion estimates of OCO-2 (-4.12 $PgC \cdot yr^{-1}$) and CarboScope (-3.46 $PgC \cdot yr^{-1}$) over the common period (2015-2020). Here, GFED 4.1 (Randerson et al., 2017) emission estimates have been used to correct the inversion estimates for fire emissions.

Comparison with OCO-2 and CarboScope inversions also indicates a substantial improvement of the global mean seasonal cycle of NEE (Fig. 5) in X-BASE compared to RS and RS+METEO. The systematic bias present in RS and RS+METEO has
295 essentially disappeared in X-BASE. The shape, and in particular the amplitude, of the global NEE seasonal cycle of X-BASE
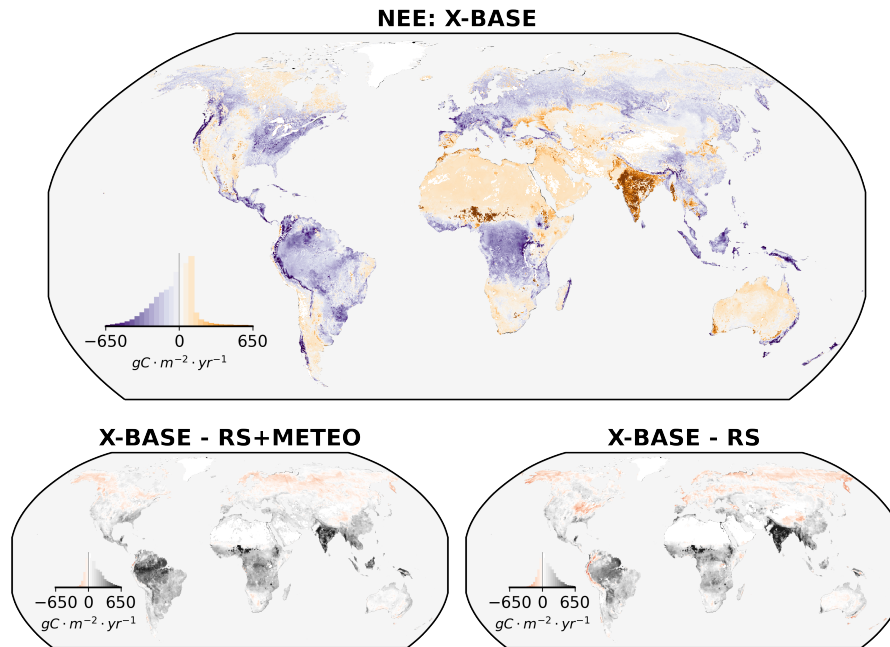
Figure 4. Comparison of annually integrated NEE **from X-BASE, RS+METEO with ERA5 forcing and RS** averaged over the period 2001-2020. The difference maps show the difference of the averages over 2001-2020.

is more consistent with the inversions. The larger and more realistic seasonal cycle amplitude of global NEE in X-BASE originates primarily from improved and increased amplitudes in boreal regions. Interestingly, X-BASE suggests slightly larger NEE seasonal cycle amplitudes in temperate regions compared to the inversions. In seasonally dry regions, the timing of maximum uptake is consistent between X-BASE and inversions, while the peak of maximum net release is larger and delayed in the inversions. In Australia, the peak of CO_2 release to the atmosphere at the end of the year present in both inversions is not evident in X-BASE, which instead shows a relatively consistent CO_2 flux to the atmosphere throughout the year. In tropical regions, the patterns of seasonal variations are qualitatively consistent between X-BASE and the previous RS and RS+METEO products. The seasonal patterns in tropical regions are relatively weak overall and seem inconsistent both between the inversions and X-BASE as well as among the inversions.

As seen in Figure 5, the X-BASE product shows the same large underestimation of globally integrated NEE inter-annual variance as the previous RS and RS+METEO products. In terms of temporal trends, the X-BASE products show almost no change in annual NEE in time, which is in contrast to the RS+METEO (slight positive trend) and RS (slight negative trend) and more consistent with the CarboScope inversions (Table C2). However, as inter-annual variability was poorly reproduced even in the cross validation (Fig. 2), trends in the X-BASE products should be taken with caution and interpreted with careful scrutiny.
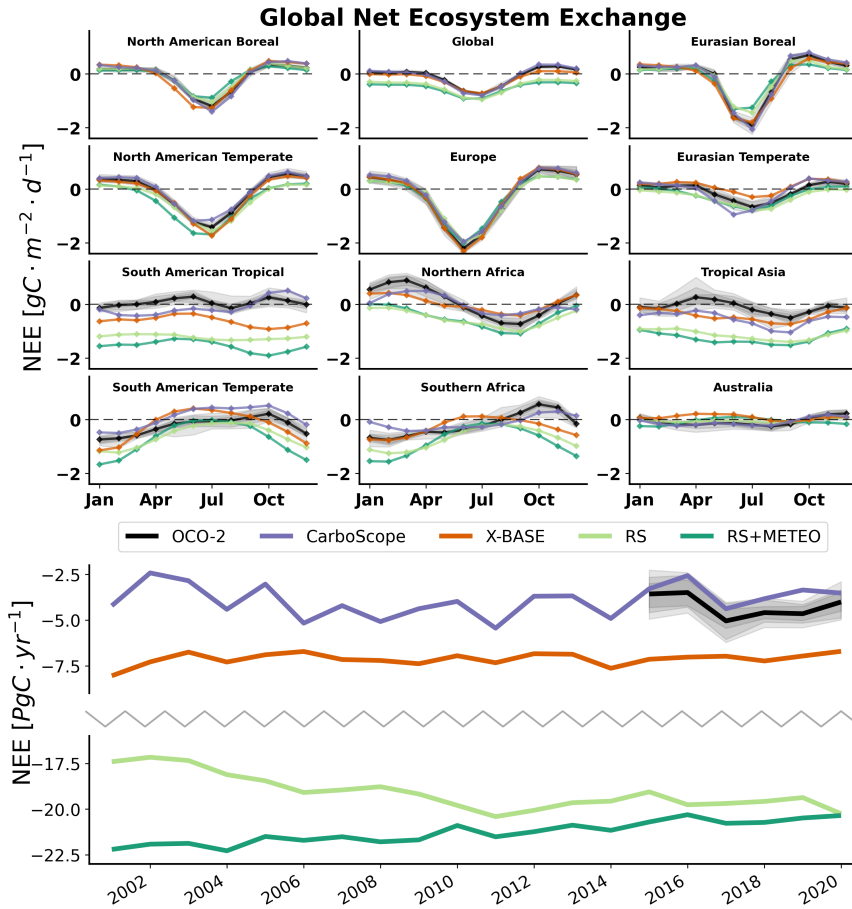
Figure 5. Seasonal and inter-annual variability of global NEE**.** Comparison of mean seasonal cycles (calculated over the common time period, 2015-2020) and inter-annual variability (2001-2020) of NEE estimated from CARBOSCOPE and OCO2 inversions as well as FLUXCOM-X-BASE and FLUXCOM RS+METEO and RS outputs. All products were integrated with a common mask that removes sparsely vegetated arid regions not predicted by RS and RS+METEO.
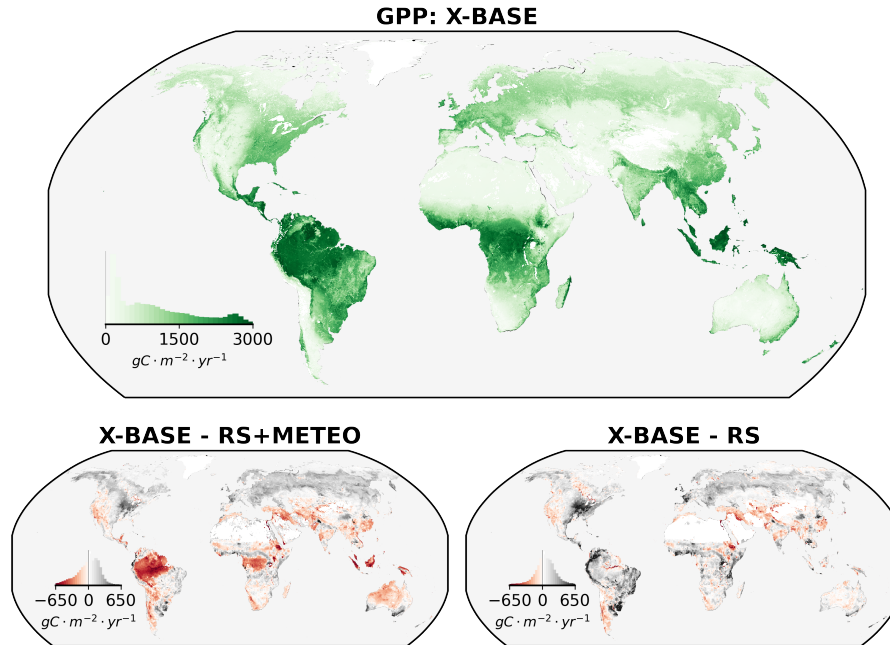
Figure 6. Comparison of annually integrated GPP **from X-BASE, RS+METEO with ERA5 forcing and RS** averaged over the period 2001-2020. The difference maps show the difference of the averages over 2001-2020.

3.2.2 Gross Primary Productivity (GPP)

X-BASE estimates the globally integrated GPP at 124.7 $\pm$ 2.1 $PgC \cdot yr^{-1}$ on average in the time period 2001-2020. Globally integrated GPP over vegetated areas (RS and RS+METEO do not have estimates for non-vegetated areas) was approximately equal for X-BASE (121.9 $\pm$ 2.1 $PgC \cdot yr^{-1}$) and RS+METEO (121.6 $\pm$ 0.4 $PgC \cdot yr^{-1}$) but considerably higher than RS

315 (113.2 $\pm$ 1.8 $PgC \cdot yr^{-1}$) over the same period. In terms of regional patterns, X-BASE GPP consistently exceeds both RS+METEO and RS in temperate, boreal, and most subtropical ecosystems, but is lower in sparsely vegetated (semi-)arid regions like southwestern North America as well as southeast Asian croplands (Fig. 6). This qualitatively consistent pattern is only broken in the humid tropics, where X-BASE GPP is higher than RS, but lower than RS+METEO.

Comparing the estimated trend over the last two decades, X-BASE GPP has a clear increasing linear trend of 0.34 $PgC \cdot$

320 yr^{-2} which is slightly higher than the trend in RS (0.25 $PgC \cdot yr^{-2}$, Table C2). In contrast, the RS+METEO product shows nearly no trend in annual GPP. The increases in both the X-BASE and RS products may be related to increases in surface greenness coming from variability in the remote sensing forcing data which are inter-annually dynamic in both products, whereas the remote sensing data were not inter-annually dynamic in the RS+METEO product which instead used only the mean seasonal cycle of the remote sensing data. The magnitude of between-year changes in globally integrated X-BASE GPP

325 is 0.575 $PgC \cdot yr^{-1}$ over the years 2001-2020, which is about twice as large as RS+METEO (0.248 $PgC \cdot yr^{-1}$), but only half the magnitude estimates in the RS set-up (1.02 $PgC \cdot yr^{-1}$, Table C2).

We further compared the temporal trajectory in GPP estimates against TROPOMI SIF as an independent proxy for GPP dynamics (Fig. 7) at a temporal resolution of 16 days. The temporal variability of X-BASE GPP strongly agrees with that in TROPOMI SIF, with squared Spearman correlation values (denoted as R^2) of the time series above 0.85 across most of the vegetated land surface (Fig. 7 top left). The only exceptions are regions with no or very small variability in both GPP and SIF such as in either evergreen tropical ecosystems in South America, Africa and southeast Asia, or sparsely to non-vegetated areas due to aridity (e.g. Mexican, and African deserts) or cold conditions (e.g. Canadian and Siberian subpolar regions). In inner Australia, despite being sparsely vegetated, variability between years is expected in GPP due to precipitation increases during La Niña years, which is however not reflected in the squared correlations. R^2 for the deviations from the average seasonality (again computed with a temporal resolution of 16 days) show the same qualitative spatial patterns (Fig. 7 top right), but are overall lower with R^2 values between 0.55 and 0.8. Anomalies of X-BASE GPP and SIF agree best in eastern European temperate forests as well as grassy and shrub ecosystems in eastern South America.

Comparison of the level of agreement of SIF and X-BASE with that of SIF and RS and RS+METEO, respectively, illustrates that X-BASE and RS GPP estimates have comparable consistency both for the time series (global area weighted mean R^2 values of 0.72 and 0.73, respectively) and anomalies (global mean R^2 values of 0.64 and 0.66, respectively). In contrast, the R^2 between RS+METEO and SIF is lower in both cases (R^2 values of 0.66 for the time series and 0.58 for anomalies). X-BASE GPP shows a higher agreement with SIF than RS both in terms of the actual trajectory and anomalies in evergreen tropical forests with no or only a very short dry season in the Amazon and Africa, as well as in fully humid parts of southeast Asia (Fig. 7 middle panel). Improvements in X-BASE GPP compared to RS are also consistent in the very continental and polar tundra areas in eastern Siberia, northern Canada and Alaska. Conversely, in arid steppe climates globally, X-BASE GPP variability agrees less with SIF than does RS GPP. X-BASE GPP variability is consistently and widespread much more similar to the variability in TROPOMI SIF than RS-METEO GPP. Increases in R^2 for X-BASE compared to RS+METEO are most pronounced in arid to semi-arid ecosystems (large parts of the Caatinga and Gran Chaco regions on South America, steppe regions in Mexico, southern and eastern Africa, Australia and central Siberia) as well as in global crop regions, especially for the deviations from the seasonality (albeit the magnitude of R^2 change is quite variable between regions, Fig. 7 bottom).

3.2.3 Water Vapor Fluxes

Globally integrated ET amounts to $74.7 \text{x} 10^3 \pm 0.9 \text{x} 10^3 \ km^3 \cdot yr^{-1}$ for 2001-2020 (Table C1) for X-BASE, with the highest rates in the tropics (Fig. 8). Comparing global totals for vegetated areas only (where all products give outputs) shows similar values for X-BASE ($68.9 \text{x} 10^3 \pm 0.9 \text{x} 10^3 \ km^3 \cdot yr^{-1}$), GLEAM ($70.9 \text{x} 10^3 \pm 0.9 \text{x} 10^3 \ km^3 \cdot yr^{-1}$) and RS+METEO ($68.3 \text{x} 10^3 \pm 0.3 \text{x} 10^3 \ km^3 \cdot yr^{-1}$) ET estimates, while the RS ET is more than 11% higher ($78.5 \text{x} 10^3 \pm 0.5 \text{x} 10^3 \ km^3 \cdot yr^{-1}$, Table C1). Particularly in evergreen tropical ecosystems, X-BASE estimates a considerably lower ET than both GLEAM, RS+METEO, and RS (Fig. 8). Furthermore, in the temperate and high latitudes of the northern hemisphere, annually integrated X-BASE ET is consistently lower than the other estimates, though the magnitude of the bias is smaller than in the tropical regions. The pattern is only reversed with higher X-BASE ET in the semi-arid and arid ecosystems of the lower and middle latitudes, especially with respect to annual ET in RS+METEO and GLEAM.
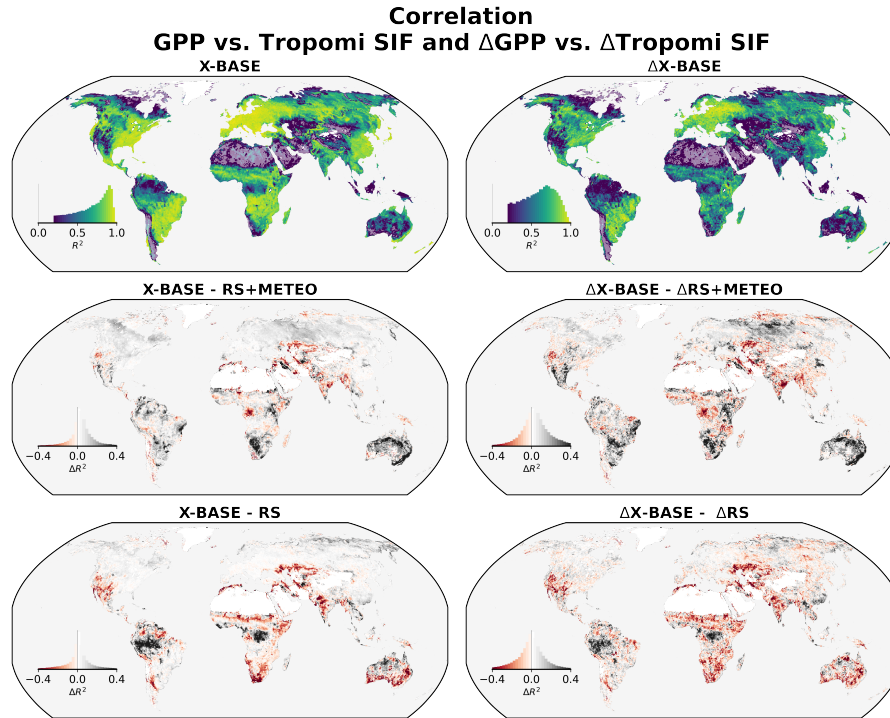
Figure 7. Similarity of temporal patterns between GPP **estimates and TROPOMI SIF observations:** R^2 (computed as the square of the Spearman correlation) between X-BASE GPP and TROPOMI SIF (Köhler et al., 2018) for the actual time series at a temporal resolution of 16 days (top left) and anomalies from the median seasonality in both variables (top right). The middle and the bottom panels relate the agreement between X-BASE GPP and TROPOMI SIF to the agreement between FLUXCOM GPP and TROPOMI SIF, where the middle panel refers to TROPOMI SIF and GPP from the RS+METEO set-up, and the bottom panel to the RS set-up. All comparisons are done for time series with a resolution of 16 days for the common time period 04/2018 to 12/2020. SIF observations have been applied a correction factor to estimate daily average SIF before aggregation. Semi-transparent areas mark pixels in which the correlation of at least one of the data sets is negative.

Comparison to precipitation estimates shows that X-BASE ET greatly exceeds precipitation inputs over large areas, indicating a strong overestimation of X-BASE ET in many arid regions with sparse vegetation (e.g. the Sahara region, Fig. C3). While transport of water both laterally (i.e. runoff from other areas) and from deeper groundwater could cause ET to exceed precipitation inputs in some areas, the extent of area where ET exceeds precipitation (e.g. the entire Sahara region) and the magnitude of the excess ET (over three times precipitation inputs) indicates a major bias in these areas and is likely due to a lack of EC data in similar ecosystems. As a rough estimate, constraining the X-BASE estimates with precipitation (see Appendix C5) suggests about 4-6x10^3 $km^3 \cdot yr^{-1}$ of water is overestimated globally.

The globally integrated ET_T amounts to 42.6x10^3 ± 1.0x10^3 $km^3 \cdot yr^{-1}$ (2001-2020) in X-BASE, resulting in an average ratio of transpiration to total evaporation of 57.0% ± 0.6% (Table C1). In contrast to ET, the ET_T estimates from X-BASE do not commonly exceed precipitation estimates (Fig. C3), which could indicate that because the water vapor flux is more tightly coupled with vegetation, the model is able to distinguish that no vegetation corresponds with no transpiration, which is not generally the case for non-transpiration evaporation. The RS and RS+METEO products did not produce ET_T estimates, so the comparison is limited to GLEAM (50.7x10^3 ± 0.6x10^3 $km^3 \cdot yr^{-1}$), which estimates ET_T on average 17% higher than X-BASE, with strong contributions from the evergreen tropics. Only in single semi-arid regions, such as northernmost Sahel as well as large parts of the South American Caatinga and Chaco regions is this pattern reversed (Fig. 8).

Spatially, X-BASE-estimated ET_T/ET exceeds 50% in the majority of areas, with the highest values seen in the higher latitude regions of Europe and Asia, as well as in subtropical ecosystems (Fig. 8). Arid regions with sparse vegetation show the lowest ET_T/ET overall, with values generally below 20%. With 71.4% ± 0.6% over global vegetated surfaces, GLEAM attributes about 10% more of its ET to ET_T than does X-BASE (Table C1). Regionally, this difference can even reach up to 40%, with the only exception being boreal forests and very dry ecosystems in the Sahel, the Arabian Peninsula and central Asia (Fig. 8).

Trends in ET, ET_T and ET_T/ET are positive and exceed the trends seen in all other estimates over the years 2001-2020. Conversely, the magnitude of inter-annual changes in X-BASE ET, ET_T, and ET_T/ET is mostly less than half than the variability in GLEAM (Table C2). Low inter-annual changes are common to the RS and RS+METEO ET as well.

Figure 9 shows the temporal correlation at 16-daily temporal scale using GLEAM as a reference, showing overall high values of squared correlation between X-BASE and GLEAM ET and ET_T (top and bottom left). Notable exceptions with low correlations are areas with low variability in ET such as the arc of deforestation, very dry areas, and tropical evergreen ecosystems in Africa. Compared to RS+METEO and RS (middle panels left column in Fig. 9), X-BASE ET temporal patterns are more similar to GLEAM ET in many areas, and especially so in areas north of the arc of deforestation and parts of tropical evergreen areas in central Africa and souteast Asia. Conversely, X-BASE ET agrees less well with GLEAM than RS or RS+METEO in the arc of deforestation itself, the eastern parts of the Amazon basin, as well as dry areas. The deviations from the mean annual cycle in ET and ET_T (right column) show overall lower correlations than the actual time series, with the highest agreement between GLEAM and X-BASE in large parts of the Amazon forest and central European ecosystems. X-BASE ET anomalies are much more strongly correlated with GLEAM ET than either RS or RS+METEO everywhere except for most (semi-)arid regions.
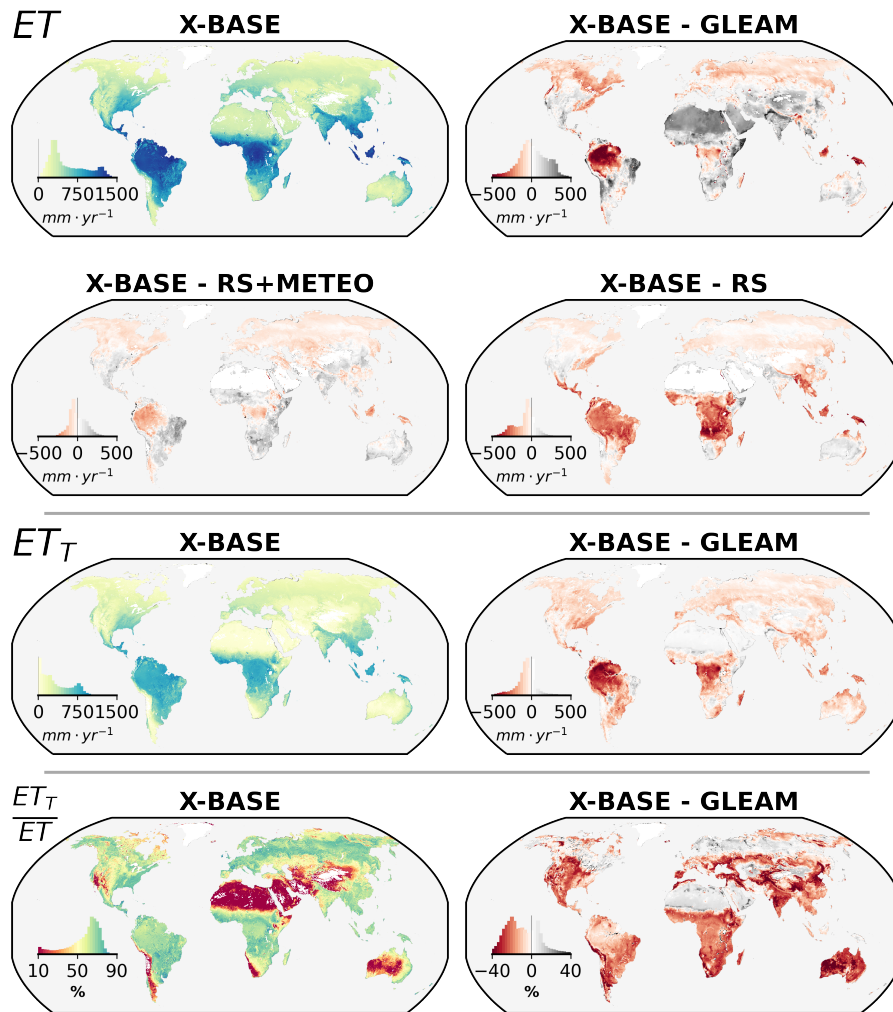
Figure 8. Comparison of evaporative flux estimates ET, ET_T **and** ET_T/ET from X-BASE and its difference with RS, RS+METEO, and GLEAM. ET_T is compared in the case of GLEAM, but is unavailable in the previous FLUXCOM ensembles.
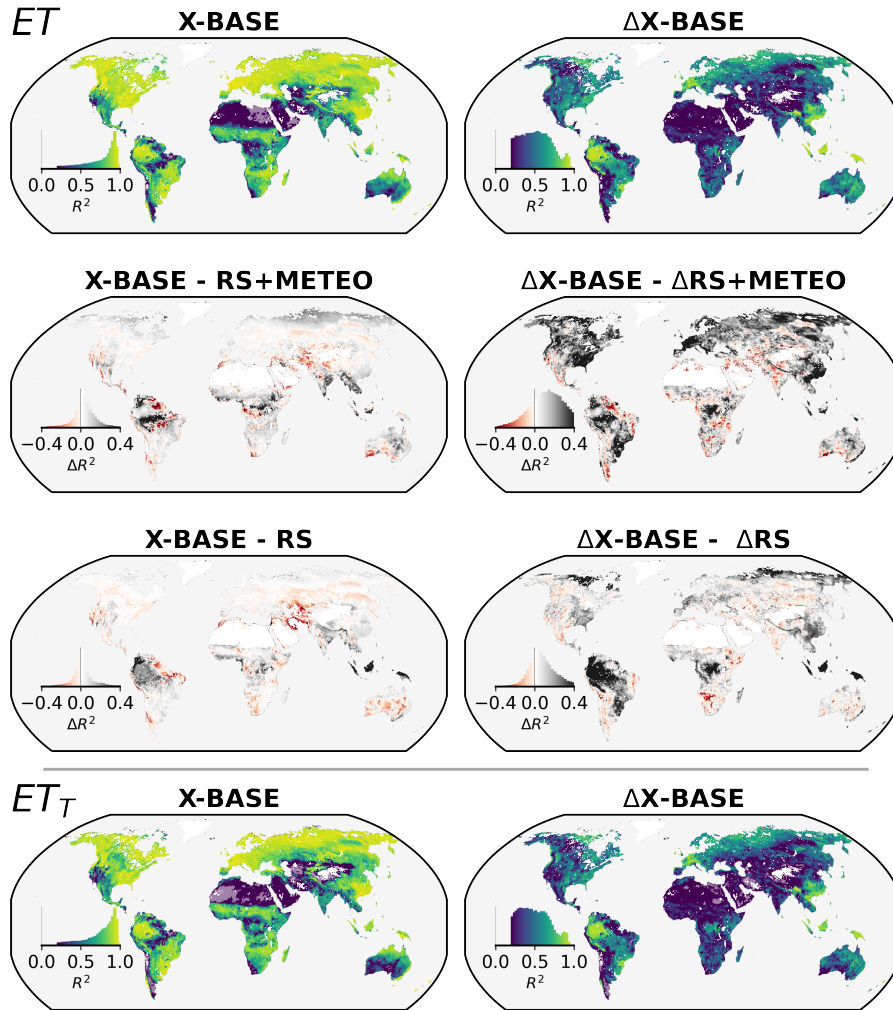
Figure 9. Similarity of temporal patterns of X-BASE an GLEAM terrestrial water fluxes in comparison to those from FLUXCOM: R^2 (computed as the square of the Pearson correlation) between X-BASE ET and GLEAM ET for the actual time series (left column) and anomalies from the median seasonality (right column). The middle panels compare the agreement between X-BASE ET and GLEAM ET to the agreement between FLUXCOM ET and GLEAM ET. The bottom panel shows the squared correlations between X-BASE and GLEAM ET_T, but no comparisons to FLUXCOM because FLUXCOM did not include ET_T. All comparisons are done for time series with a resolution of 16 days and 0.05 degrees for the years 2001-2020. Semi-transparent areas mark pixels in which the correlation of at least one of the data sets is negative.

4 Discussion

We have presented qualitative and quantitative comparisons of the X-BASE products with previous FLUXCOM estimates and independent data sets where possible. Statements on the main causes of (dis-)agreements in the magnitude and spatiotemporal variability in the flux estimates remain speculative as detailed analyses would require further investigation in the form of experiments, which is beyond the scope of this manuscript. In the following we discuss the prominent changes in NEE compared to FLUXCOM as a key scientific highlight in X-BASE and outline potential ways forward to tackle persistent challenges in empirical upscaling.

4.1 Higher consistency of NEE with atmospheric carbon cycle constraints

Although FLUXCOM-X follows the same fundamental approach as FLUXCOM, we find a substantial improvement of the magnitude of the annually integrated NEE of FLUXCOM-X-BASE over previous FLUXCOM products (Jung et al., 2020) when compared to independent estimates from atmospheric inversions. The mean global X-BASE NEE of -5.75 $PgC \cdot yr^{-1}$ is slightly smaller than the inferred NEE of -3.92 $PgC \cdot yr^{-1}$ (corrected for fire emissions based on GFED 4.1) from CarboScope. The remaining difference could easily be explained by carbon sources such as aquatic evasion and volatile organic compounds that are included in the atmospherically based estimate but not in eddy-covariance based FLUXCOM (see Jung et al. (2020) and Zscheischler et al. (2017) for further discussion).

The improved global NEE of FLUXCOM-X-BASE originates most likely from enhanced quality of eddy covariance measurements in the training resulting from years of consistent improvements in instrumentation, method development, and quality assurance from the point of measurement to the synthesis datasets. Previous up-scaling-based NEE products of Jung et al. (2011, 2020); Bodesheim et al. (2018) - all based on the La Thuile FLUXNET dataset but varying with respect to machine learning methods, predictor variables, and temporal resolution - consistently estimated a nearly three-fold larger global terrestrial carbon uptake compared to X-BASE. As discussed and speculated in Jung et al. (2020), La Thuile likely contained biased NEE measurements, in particular for some tropical sites (Fu et al., 2018), and together with the sparsity of data in the tropics, these biases were propagated to unrealistic tropical and global NEE estimates. The fact that we can now reconcile bottom-up global eddy-covariance-based NEE and estimates from top-down atmospheric inversions is a major achievement of the FLUXNET community. For context: 1 $PgC \cdot yr^{-1}$ over the global vegetated area ($145 \times 10^6 km^2$) corresponds to ~7 $gC \cdot m^2 \cdot yr^{-1}$, which marks a challenge for achieving such accuracy of mean NEE at any one flux tower site. The lesson learned here emphasizes once more that it is crucial to control for and minimize systematic biases of in-situ eddy covariance measurements (Moncrieff et al., 1996).

The improved seasonality of X-BASE NEE, in particular for boreal regions, likely also results from enhanced information in the training data due to the hourly resolution. Similar improvements were observed in Bodesheim et al. (2018) who extended RS+METEO by training on half-hourly flux observations. The hourly resolution improves the seasonal high-latitude NEE likely due to better capturing the responses to light when daylength varies strongly.

4.2 New opportunities by X-BASE products

The improvements of NEE make X-BASE attractive as a data-driven biogenic prior for atmospheric inversions (Munassar et al., 2022). Moreover, its hourly resolution facilitates better integration in inversion systems due to the accounting of diurnal flux and atmospheric transport variations, while its high spatial variations can provide patterns of flux variations that cannot be resolved by atmospheric constraints alone.

For the first time, X-BASE includes a global data-driven product of ecosystem transpiration. The estimated global ET_T/ET ratio of 57% is consistent with independent top-down assessments from isotope base methods (Good et al., 2015; Coenders-Gerrits et al., 2014) and past up-scaling estimates (Wei et al., 2017; Schlesinger and Jasechko, 2014). The spatially and temporally high resolution data-driven X-BASE ET_T product provides a valuable complementary perspective to simulations from process-based land surface models, which show large disagreements and often indicate global ET_T/ET below 50% (Berg and Sheffield, 2019; Miralles et al., 2016). This advancement opens new opportunities for large scale studies of carbon- water relations on a diurnal time scale. The generation of the X-BASE ET_T product was facilitated by the development of site-level evapotranspiration partitioning methods (Nelson et al., 2018, 2020) underlining once more the importance of advances by the FLUXNET community for Earth system science.

5 Tackling persistent challenges

Next to the improvements and opportunities that X-BASE brings through the enhancement in site-level training data quality and quantity as well as the higher spatiotemporal resolution, we find that some key issues previously identified in FLUXCOM (Tramontana et al., 2016; Jung et al., 2020; Bodesheim et al., 2018) persist in X-BASE. These include 1) the insufficient representation of water-related effects, 2) the limited predictability of the spatial patterns of mean NEE, as well as 3) severe limitations with respect to the variability between years and over decades. In the following, we outline what we consider the most promising ways forward to tackle these (partly interrelated) challenges in future developments beyond X-BASE: novel additional predictor variables, more in-situ observations especially for some key ecosystems as well as innovative approaches of constraining machine learning models.

The persistent challenge and importance of capturing water effects on land-atmosphere flux variations is illustrated by the overestimation of mean ET in very dry, sparsely vegetated areas (Fig. C3), as well as by the poorer consistency of NEE seasonality with inversions in water limited regions (Fig. 5). For GPP temporal patterns we find that X-BASE shows improved agreement with SIF in water limited regions compared to RS+METEO (Fig. 7), which is likely because X-BASE uses concomitantly changing remote sensing observations opposed to a mean seasonal cycle only in RS+METEO. However, X-BASE shows deteriorated agreement with SIF when compared to RS, even though X-BASE was trained on hourly flux observations with improved coverage of dry conditions (Fig. 1). This decrease in performance indicates clearly the importance and uncertainty related to the predictor variable set for capturing water related effects. Uncertainties due to water limitation effects are also seen in the divergence of ET and ET_T estimates is semi-arid regions such as the Sahel and South American Caatinga (Figs. 8 and 9). Thus, there is considerable potential for advancements by including remote sensing based predictors on soil

moisture, sub-daily varying land surface temperature from geostationary satellites, SIF, and vegetation optical depth. Here, key challenges reside in achieving a sensible integration of flux observations with footprints that are much smaller than corresponding Earth observation products on the one hand, and an integration of disparate Earth observation products with each other on the other hand. This is one research priority for further FLUXCOM-X developments.

465 Missing predictor variables is likely also a main reason for the limited skill of predicting between site variability of mean NEE (Fig. 2), which can depend on legacy effects of disturbances and management that are not accounted for. Novel and complementary Earth observation products that characterise ecosystem structure and states related to biomass and canopy heights from SAR and LIDAR should help raise the accuracy of FLUXCOM-X based mean NEE in future efforts. Also high resolution Earth observation products such as from Landsat may help to better resolve spatial details. X-BASE shows a

470 prominent pattern of carbon flux to the atmosphere in sub-tropical and crop dominated regions of India and the Sahel, which emphasizes the need to improve in-situ data coverage for agricultural systems, especially outside the temperate zone, and including important meta-data to better characterize these ecosystems and their site history. Despite the greatly reduced overall bias of mean NEE, we emphasize that X-BASE products are pre-mature for diagnosing spatial variations of mean NEE.

 The representation of longer term dynamics remains an area with opportunity for improvements in X-BASE. Inter-annual

475 variability is still poorly reproduced in cross validation (Fig. 2), particularly for NEE, which is likely not only due to the complexity of processes shaping inter-annual variations but also due to temporal discontinuities in flux tower time series related to changes in instrumentation and factors like management (Jung et al., 2024) that are not accounted for. The complexities of relying on field deployed instrumentation, together with the uncertainties related to linking satellite and flux data, causes poor signal to noise ratios and may impede good cross-validation results for i.a.v.. Globally, comparisons of X-BASE with inversions

480 reveal an underestimated inter-annual variance and a poor correlation for global NEE i.a.v. (Fig. 5 and Table C2). Interestingly, X-BASE GPP shows improved correspondence with SIF anomalies compared to RS+METEO, especially in water limited regions (Fig. 7), while no such improvement is evident for global NEE, which is likely due to the compensatory water effects in the global NEE signal (Jung et al., 2017). That a comparison of RS+METEO runs with different meteorological forcing data showed the weakest correspondence with inversion i.a.v. when using ERA5 (Jung et al., 2020) explains the substantially

485 better correlations of RS+METEO with inversions for NEE i.a.v. in earlier studies (Jung et al., 2017, 2020), and may also explain the poor correlation of X-BASE. Thus, testing if alternative meteorological forcing data can improve global NEE i.a.v. for X-BASE is an important next step. It remains unclear at this point if accurate inter-annual variations at site-level and globally can be achieved by the FLUXCOM approach in the near future. Additional constraints beyond FLUXNET such as atmospheric CO_2 measurements (Upton et al., 2023) or theoretical considerations in the form of hybrid (Reichstein et al.,

490 2019) or deep learning models (Camps-Valls et al., 2021) are promising and we will foster such endeavours.

6 Conclusions

We presented X-BASE, a new set of global high-resolution data-driven products of land-atmosphere fluxes from the FLUX-COM approach. This represents a cornerstone of our developments of the FLUXCOM-X framework designed to explore and

mitigate current limitations to up-scaling from site to global scale. Improvements of the eddy covariance data facilitated reconciling estimates of global terrestrial net carbon exchange from X-BASE with top-down atmospheric inversions, and allowed for the first time the generation of a global data-driven estimate of ecosystem transpiration. Beyond fostering all activities to enhance quality and coverage of available flux tower observations, most promise for future advancements by FLUXCOM-X relates to the synergistic exploitation of complementary satellite data streams to better capture water-related, site-history, and management effects. This will be challenging as it requires developing strategies and methodologies to better integrate in-situ flux observations and spaceborne Earth observations with very heterogeneous acquisition properties and with spatial resolutions that are often very coarse compared to flux tower footprints. The recent de-orbiting of the TERRA spacecraft requires employing alternative satellite missions where practical issues of data acquisition and conceptual issues related to temporal consistency and reduced overlap with FLUXNET records pose imminent challenges. With FLUXCOM-X we have prepared the ground for tackling these challenges which can facilitate up-to-date and accurate flux estimates and thereby contribute to increased understanding of the Earth system in the future.

Appendix A: Naming conventions

Names of products and modelling environments may create confusion, especially given the legacy of FLUXCOM. We therefore will follow the following naming conventions and require potential users of products and collaborators to also follow this convention.

FLUXCOM	a data-driven modelling intercomparison initiative creating ensembles of carbon, water and energy fluxes by varying the meteorological forcing and the machine learning method. Two sets of data ensembles were created, and it is important to differentiate these and properly refer to these as they differed in the predictor variables and the spatiotemporal resolution. The implementation of FLUXCOM was strongly tailored towards these two ensembles and the training data mainly consisted of the La Thuile Fluxnet data release.
FLUXCOM 'RS'	one of the FLUXCOM ensembles. It is characterized by using only predictors based on remote sensing (from the MODIS sensors) and has a fixed resolution of 8 days and 0.083deg. The ensemble members are created by varying the machine learning method.
FLUXCOM 'RS+METEO'	the other one of the FLUXCOM ensembles and is characterized by using only a mean seasonality of satellite observations (also from the MODIS sensors) but additional meteorology as predictors. The data products have a fixed resolution of 0.5deg and daily. The ensemble members consist of combinations of different machine learning methods and meteorological data sets.
FLUXCOM-X	the name of the newly implemented modelling environment that we introduce here. FLUXCOM-X follows the same overall principles like FLUXCOM, but unlike FLUXCOM, FLUXCOM-X was not tailored to specific input data (and hence their size, resolution, etc.), but has been built with the intention of allowing full flexibility in all methodological choices in the empirical upscaling process while being computationally scalable.
X-BASE	the name of the first basic set of data products produced with FLUXCOM-X. X-BASE products encompass NEE, GPP, ET, and ET_T, and have a native resolution of $0.05°$ every hour over the years 2001-2021. X-BASE products are driven by both meteorological predictors and remotely sensed observations from the MODIS sensors.

X-[*name*]	FLUXCOM-X is expected to produce a lot of different flux estimates which will differ in decisive methodological choices. All data products produced from FLUXCOM-X shall be named following the convention X-[specific name].

Appendix B: Details on processing of Earth Observation Data

B1 Dynamic quality control and cutout size

The conditions in the pixels around a given EC station should best represent the conditions of the land surface in the area where the actual fluxes originate from. Given that the actual flux footprints are not generally available or computable for lack of critical information, we assume that the pixel containing the actual EC station (the 'tower pixel') is most representative for the dynamics of the area of influence on a tower. However, data availability and quality in the tower pixel is often insufficient. An iterative approach therefore selects both the cutout size and the strictness of the BRDF inversion quality from within defined bounds in a way that maximizes data availability and that ensures representativeness of the spatially averaged time series for the given site at the same time. In more detail, we start with a strict criterion for BRDF inversion quality (BRDF_Albedo_Band_Quality_Bandx flag in MCD43A2 <= 2, meaning only full inversions). Then three options regarding the cutout size are considered:

A) only the tower pixel,
B) those 20% of pixels within 4x4 km^2 around a tower that are best correlated with the tower pixel are linearly regressed against the tower pixel and subsequently spatially averaged,
C) the 25% of pixels within a 4x4 km^2 area that are closest to the tower are averaged with the inverse of the distance to the tower as weight.

The criteria for selection between options A-C is based on the number of available good quality observations n in the resulting spatial average time series per site as follows:

```
if (n_A >= 60 %) & (n_B <= 70 %):
    select A
elif (n_A >= 60 %) & (n_B >= 70 %):
    select B
elif (n_A < 60 %) & (n_A > 15 %):
    select B
else:
    select C
```

If after the previous steps still less than 40% of good quality observations outside of snow covered times are available in the resulting average time series for a given site and index, the BRDF inversion quality threshold is relaxed to also allow magnitude

inversions (MCD43A2 BRDF inversion quality flag <= 3), and the procedure to select the pixels contributing to the average described above is repeated. Consequently, the size of the area that a MODIS reflectance time series represents varies between
540   sites, and so does the BRDF inversion quality.

For the global gridded MODIS data, the BRDF inversion quality is consistently selected as <=2 or <=3 based on the number of available good quality observations in a pixel.

B2   Details on the treatment of land cover information

Land cover information was passed through an intermediary classification system to both act as an encoding mechanism and to
545   allow for arbitrary links between classification schemes. Rather than simple true/false classification for each category, different attributes are classified based on whether the classification has (value=1.0), might have (value=0.5), does not have (value=0.0) a specific feature, or is unknown (value=-1.0). In the specific case of the MCD12C1 classification scheme, the conversion is as seen in table B1.

Table B1: **Land cover intermediary classification encoding for MCD12C1 classifications** where the classification has (value=1.0), might have (value=0.5), or does not have (value=0.0) a specific feature, or is unknown (value=-1.0).

	ENF	EBF	DNF	DBF	MF	CSH	OSH	WSA	SAV	GRA	SNO	CRO	WET
Trees	1	1	1	1	1	0.5	0	1	0.5	0	-1	0	0
Shrubs	0	0	0	0	0	1	1	0.5	0.5	0	-1	0	0
Grasses	0	0	0	0	0	0	0.5	0.5	1	1	-1	0	0
Crops	0	0	0	0	0	0	0	0	0	0	-1	1	0
Unveg	0	0	0	0	0	0	0.5	0	0	0	0	0	0
Water	0	0	0	0	0	0	0	0	0	0	0.5	0	1
Wetland	0	0	0	0	0	0	0	0	0	0	1	0	0
C4_photo	0	0	0	0	0	-1	-1	-1	-1	-1	0	-1	0
Managed	-1	-1	-1	-1	-1	-1	-1	-1	-1	-1	0	1	0
Needleleaf	1	0	1	0	-1	-1	-1	-1	-1	0	-1	0	0
Broadleaf	0	1	0	1	-1	-1	-1	-1	-1	0	-1	0	0
Deciduous	0	0	1	1	-1	-1	-1	-1	-1	0	-1	0	0
Evergreen	1	1	0	0	-1	-1	-1	-1	-1	0	-1	0	0

B3 Overview of XGBoost hyperparameters used

hyperparameter	value used
num_boost_round	1000
early_stopping_rounds	10
colsample_bynode	1
learning_rate	0.05
max_depth	10
num_parallel_tree	1
objective	reg:squarederror
subsample	0.6666666666666666
tree_method	hist
min_child_weight	5
tree_method	hist
min_child_weight	5

 Appendix C: Additional results

C1 Additional cross-validation results
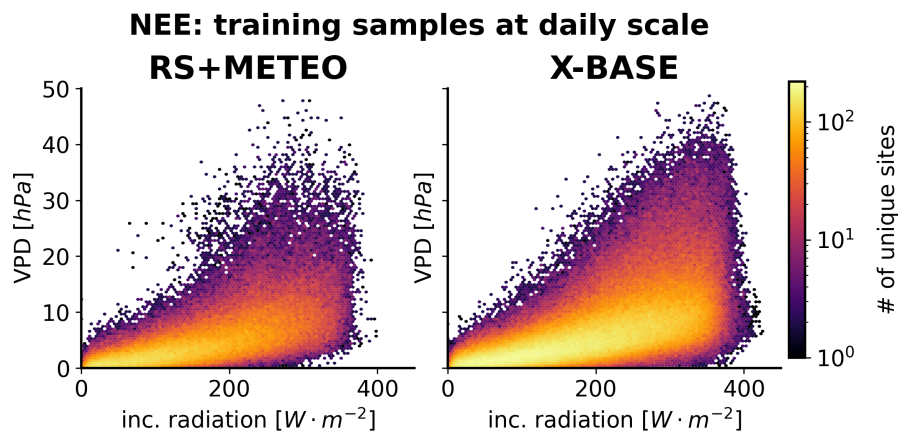
Figure C1. Cross-validation sampling in meteorological space: Number of unique sites contributing to sampling for NEE for FLUXCOM RS+METEO (left) compared to the sampling in the X-BASE set-up (right). Color corresponds to number of unique sites per bin in log scale.

C2 Large carbon release in tropical croplands
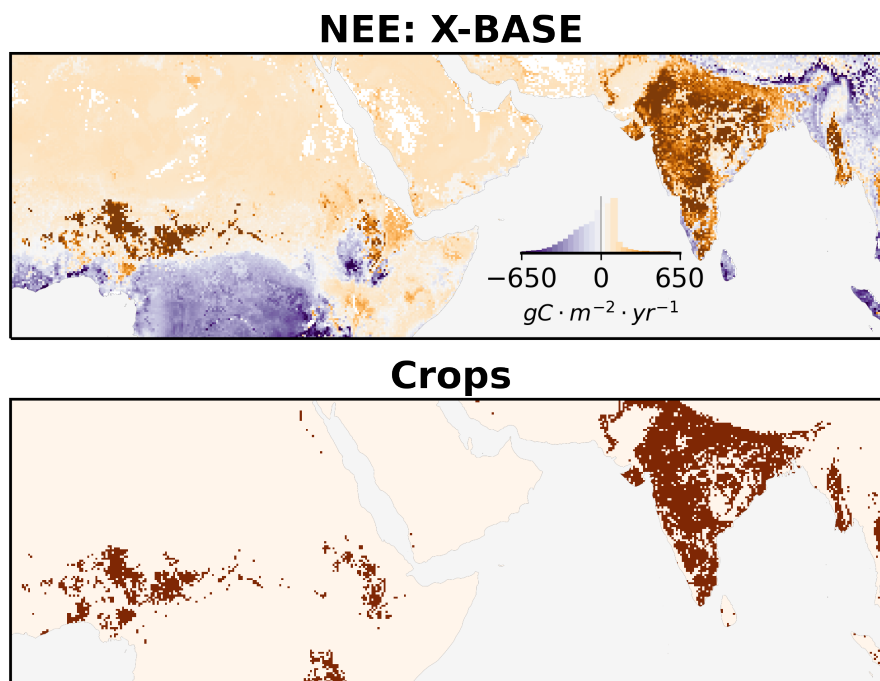
Figure C2. Large carbon release in tropical croplands

C3   Global magnitude of all fluxes

Table C1: **Global magnitude of all fluxes.** Column *Global Total* is the globally integrated flux for all areas including sparsely vegetated dry areas from 2001-2020. The column *Veg. Areas* includes a common mask which removes sparsely vegetated areas which are not computed for the RS and RS+METEO products. Values reported after the $\pm$ correspond to the standard deviation across years.

	Global Total	Veg. Areas
NEE		
	$PgC \cdot yr^{-1}$	$PgC \cdot yr^{-1}$
X-BASE	-5.75 ± 0.33	-7.12 ± 0.32
RS+METEO	-	-21.27 ± 0.59
RS	-	-19.08 ± 0.93
CarboScope	-3.88 ± 0.84	-3.92 ± 0.84
GPP		
	$PgC \cdot yr^{-1}$	$PgC \cdot yr^{-1}$
X-BASE	124.7 ± 2.1	121.9 ± 2.0
RS+METEO	-	121.6 ± 0.4
RS	-	113.2 ± 1.8
ET		
	$km^3 \cdot yr^{-1}$	$km^3 \cdot yr^{-1}$
X-BASE	$74.7 \times 10^3 \pm 0.9 \times 10^3$	$68.9 \times 10^3 \pm 0.9 \times 10^3$
RS+METEO	-	$68.3 \times 10^3 \pm 0.3 \times 10^3$
RS	-	$78.5 \times 10^3 \pm 0.5 \times 10^3$
GLEAM	$72.5 \times 10^3 \pm 1.0 \times 10^3$	$70.9 \times 10^3 \pm 0.9 \times 10^3$
ET$_T$		
	$km^3 \cdot yr^{-1}$	$km^3 \cdot yr^{-1}$
X-BASE	$42.6 \times 10^3 \pm 1.0 \times 10^3$	$41.8 \times 10^3 \pm 0.9 \times 10^3$
GLEAM	$50.7 \times 10^3 \pm 0.6 \times 10^3$	$50.7 \times 10^3 \pm 0.6 \times 10^3$
ET$_T$/ET		
X-BASE	$57.0\% \pm 0.6\%$	$60.7\% \pm 0.6\%$
GLEAM	$70.0\% \pm 0.6\%$	$71.4\% \pm 0.6\%$

C4 Linear trends and inter-annual variability for all fluxes

Table C2: **Long-term variability of fluxes.** Column *linear trend* is the linear slope of annually integrated fluxes over the years 2001-2020. The column *inter-annual variability* is computed as the standard deviation of annually integrated fluxes after the trend is removed.

	Linear Trend	Inter-annual Variability
NEE		
	$PgC \cdot yr^{-2}$	$PgC \cdot yr^{-1}$
X-BASE	0.017	0.306
RS+METEO	0.095	0.229
RS	-0.129	0.557
CarboScope	0.006	0.837
GPP		
	$PgC \cdot yr^{-2}$	$PgC \cdot yr^{-1}$
X-BASE	0.340	0.575
RS+METEO	-0.053	0.246
RS	0.248	1.023
ET		
	$km^3 \cdot yr^{-2}$	$km^3 \cdot yr^{-1}$
X-BASE	0.144×10^3	0.331×10^3
RS+METEO	-0.010×10^3	0.301×10^3
RS	0.053×10^3	0.392×10^3
GLEAM	0.102×10^3	0.730×10^3
ET$_T$		
	$km^3 \cdot yr^{-2}$	$km^3 \cdot yr^{-1}$
X-BASE	0.158×10^3	0.277×10^3
GLEAM	0.035×10^3	0.596×10^3
ET$_T$/ET		
	$\% \cdot yr^{-1}$	$\%$
X-BASE	0.102%	0.157%
GLEAM	-0.054%	0.452%

C5 Potential overestimation of ET in dryland areas

Maps in Fig. C3 show the extend where ET and ET_T exceed precipitation as the ratio between the total of each flux to total precipitation (from GPCC Schneider et al. (2022)). Overall, X-BASE ET largely exceeds precipitation in most dry, sparsely vegetated areas, indicating overestimation. In contrast, ET_T does not show such extensive overestimation, limited instead to only smaller regions of the Sahara.

The amount of overestimation of X-BASE ET can be roughly estimated by replacing areas where annual ET exceeds precipitation inputs with the corresponding annual precipitation inputs for each grid cell, i.e. replacing areas where the $ET/precip$ ratio is more than a threshold with the precipitation rather than the estimated ET. Using thresholds from 1.25 to 2.5 gives an excess of ET (i.e. original ET minus precipitation corrected) from 3.9x10^3 to 6.1x10^3 $km^3 \cdot yr^{-1}$.

X-BASE ET ratio to Precip.
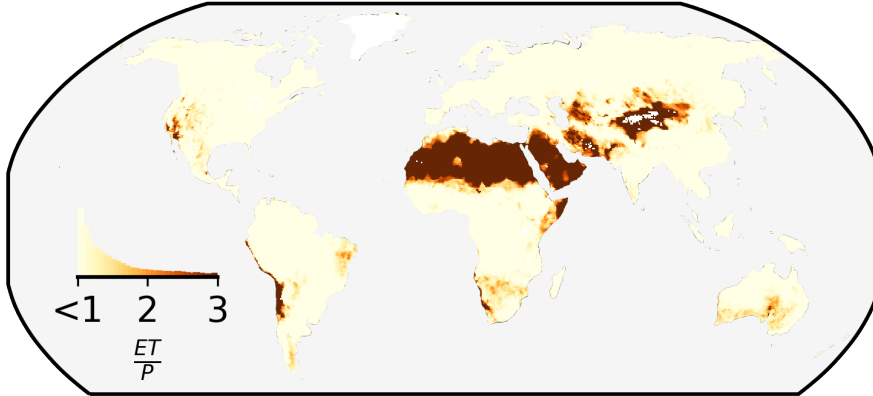
X-BASE ET$_T$ ratio to Precip.
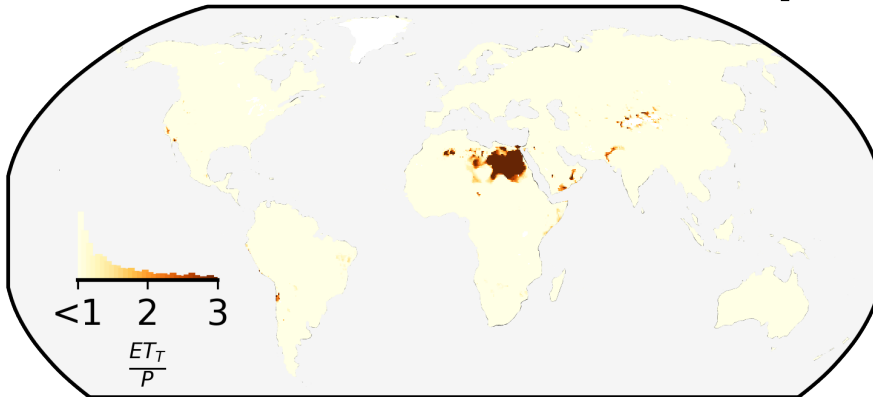
Figure C3. Potential ET **overestimation** based on the ratio of estimated ET to precipitation from the Global Precipitation Climatology Centre (GPCC Schneider et al. (2022)).

Data availability. All data FLUXCOM-X-BASE data covering the years 2001-2021 (this manuscript only shows 2001-2020) is available as
565 aggregated NetCDF file formats, to ease data handling for common use cases, from the ICOS Carbon Portal (https://doi.org/10.18160/5NZG-JMJE). Furthermore, the full resolution data is accessible in the zarr format and in a publicly available object store provided by German Climate Computing Center (Deutsches Klimarechenzentrum, DKRZ). Instructions on how to all data, as well as the full dataset, can be found at the associated repository (https://gitlab.gwdg.de/fluxcom/fluxcomxdata).

Author contributions. JN, SW and MJ wrote the manuscript, and all authors contributed to the editing and structuring of it. JN, SW, FG, BK,
570 ZH wrote the code which constitutes the modelling environment FLUXCOM-X, structuring it according to discussions including MJ, UW, GD, and MM. Editorial input was provided by AI, AK, AK, AS, BB, BK, DB, DP, FT, GCV, GD, GN, GW, JA, JC, KI, KMK, KN, LH, LS, MK, MM, MR, NB, RLS, SS, TT, and WZ. All other authors contributed through their work at one or more eddy-covariance stations through the acquisition of funding, set-up and maintenance, pre-processing and quality control, administration, and their insertion into regional or global networks.

575 *Competing interests.* We declare that one or more of the coauthors of this manuscript is a member of the editorial board of Biogeosciences.

Acknowledgements. We would like to thank the broader eddy covariance community, including FLUXNET and the associated regional networks, particularly the European Integrated Carbon Observation System (ICOS) and AmeriFlux. We also acknowledge the contributions of Andrej Varlagin and colleagues to these efforts. We thank the team at the ICOS Carbon Portal for their support in publishing the FLUXCOM-X data sets, with great thanks in particular to Ute Karstens and Zois Zogopoulos. We also thank Brendan Byrne and colleagues
580 of Jet Propulsion Laboratory, California Institute of Technology, Pasadena, CA, USA for use of the OCO2 data.

The work of S. Walther, J. A. Nelson and M. Jung was funded in part by European Union's Horizon 2020 research and innovation program (grant no. 776186 CHE, 776810 VERIFY, 958927 CoCO2,820852 E-SHAPE). S. Walther acknowledges funding from an European Space Agency Living Planet Fellowship in the project Vad3e mecum as well as the CCI LST project (4000123553/18/I-NB). G. Duveiller and
585 Z. M. Hamdi acknowledge funding from the European Space Agency in the Sen4GPP project (4000134598/21/I-NB). S. Sabbatini and G. Duveiller acknowledge Horizon Europe funding (Open Earth Monitor Cyberinfrastructure project, 101059548). D. Zona acknowledges NSF award numbers 2149988 and 1932900. A. Klosterhalfen and A. Knohl acknowledge funding by the German Federal Ministry of Education and Research (BMBF) as part of the European Integrated Carbon Observation System (ICOS), by the Deutsche Forschungsgemeinschaft (INST 186/1118-1 FUGG) and by the Ministry of Lower-Saxony for Science and Culture (DigitalForst: Niedersächsisches Vorab (ZN
590 3679)). L. Montagnani acknowledges funding provided by Forest Services, Autonomous Province of Bolzano. E. Yepez acknowledges that MX-Tes is part of the MexFlux regional network. Funding for the Swiss sites is greatly acknowledged from various sources: from the EU project SUPER-G (contract no. 774124), the SNF projects M4P (40FA40_154245), DiRad (146373), InnoFarm (407340_172433), CoCo (200021_197357), ICOS-CH (20FI21_148992, 20FI20_173691, 20FI20_198227) and InsuranceGrass (100018L_200918), from NESTLE via the ETH foundation (DONA), from the ETH Board and from ETH Zurich (project FEVER ETH-27 19-1). Funding for US-BZB, US-

BZF, US-BZo, and US-BZB was provided by National Science Foundation Grants DEB LTREB 1354370 and 2011257, DEB-0425328, DEB-0724514, and DEB-0830997, as well as funding by the US Geological Survey Climate R&D program. Bonanza Creek Long Term Experimental Research station provided lab space, equipment. US-ICs and US-ICt were supported by the grants from the Arctic Observatory Program of the National Science Foundation (grant numbers 1936752, 1503912, 1107892). S. Aranda-Barranco acknowledges the projects PID2020-117825GB-C21 and PID2020-117825GB-C22 funded by MCIN/AEI/10.13039/501100011033, as well as support by the FPU grant by the Ministry of Universities of Spain (REF: FPU19/01647). SE-Deg, SE-Svb and SE-Ros acknowledge funding from the Swedish Research Council, and contributing research institutes to the Swedish Integrated Carbon Observation System (ICOS-Sweden) Research Infrastructure and the Swedish Infrastructure for Ecosystem Science (SITES). T. Tagesson was funded by the Swedish National Space Agency (SNSA Dnr 2021-00144), and FORMAS (Dnr. 2021-00644). W. Woodgate is supported by an Australian Research Council DECRA Fellowship (DE190101182). I. Mammarella acknowledges funding from Academy of Finland (N-PERM 341349), ICOS-Finland UH, EU projects (GreenFeedback 101056921, LiweFor). D. Vitale acknowledges the Integrated Carbon Observation System - Research Infrastructure (ICOS ERIC, https://www.icos-cp.eu/) and the ICOS ETC funding from the Italian Ministry of Research. M. Göckede was supported by the European Research Council (ERC) under the European Union's Horizon 2020 research and innovation programme (grant agreement No 951288, Q-Arctic). The DE-Geb site received funds within the ICOS Germany preparatory and implementation phase by the Federal Ministry of Education and Research and is supported by the Ministry of Digital and Traffic through ICOS station contributions as well as by the Ministry of Food and Agriculture covering operational costs. G. Gerosa thanks the Catholic University of Brescia for continuous supporting the research station of Bosco Fontana (ICOS station IT-Bft). L. Šigut acknowledges support by the Ministry of Education, Youth and Sports of CR within the CzeCOS program (grant number LM2023048) and AdAgriF project (CZ.02.01.01/00/22_008/0004635). G. Camps-Valls, M. Reichstein, B. Kraft, and G. Duveiller acknowledge funding by the European Research Council (ERC) Synergy Grant "Understanding and modeling the Earth System with Machine Learning (USMILE)" under the Horizon 2020 research and innovation programme (Grant agreement No. 855187). A. Desai acknowledges the US Dept of Energy American Network Management Project award to ChEAS core site cluster (US-PFa, US-WCr, US-Syv, US-Los), Wisconsin Potato and Vegetable Growers Association and WI Dept of Natural Resources (US-CS*), NSF 1822420, 2313772 (US-PFa). M. Roland and B. Gielen acknowledge the Research Foundation Flanders (FWO) for the support of ICOS research infrastructure in Flanders, Belgium. D. Papale thanks the support of the ITINERIS - Italian Integrated Environmental Research Infrastructures System project (IR0000032) funded by Next Generation EU Mission 4.2.3.1. T. Vesala acknowledges ICOS-Finland (University of Helsinki) and Flagship funding (grant no. 337549). T. Sachs acknowledges that the DE-Zrk site relies on infrastructure of the Terrestrial Environmental Observatories Network (TERENO) supported by a Helmholtz Young Investigators Grant (VH-NG-821). E. Pendall acknowledges Australian Terrestrial Ecosystem Research Network, as part of the National Cooperative Research Infrastructure System. S. Knox was also support by an NSERC Discovery Grant (RGPIN-2019-04199) and Alliance Grant (ALLRP 555468-20). H. Kobayashi acknowledges ArCSII No. JPMXD1420318865 (US-Prr). S. Metzger acknowledges the National Ecological Observatory Network, which is a program sponsored by the National Science Foundation and operated under cooperative agreement by Battelle. This material is based in part upon work supported by the National Science Foundation through the NEON Program. B. Heinesch and C. Vincke acknowledge the Service Public de Wallonie (SPW-DGO6) for the support of ICOS research infrastructure in Wallonia, Belgium.

References

Amiro, B.: FLUXNET2015 CA-SF2 Saskatchewan - Western Boreal, Forest Burned in 1989, 2016a.

630   Amiro, B.: FLUXNET2015 CA-Man Manitoba - Northern Old Black Spruce (Former BOREAS Northern Study Area), 2016b.

Amiro, B.: FLUXNET2015 CA-SF1 Saskatchewan - Western Boreal, Forest Burned in 1977, 2016c.

Amiro, B.: FLUXNET2015 CA-SF3 Saskatchewan - Western Boreal, Forest Burned in 1998, 2016d.

Ammann, C.: FLUXNET2015 CH-Oe1 Oensingen Grassland, 2016.

Arain, M.: AmeriFlux FLUXNET-1F CA-TPD Ontario - Turkey Point Mature Deciduous, 2022a.

635   Arain, M.: AmeriFlux FLUXNET-1F CA-TP3 Ontario - Turkey Point 1974 Plantation White Pine, 2022b.

Arain, M. A.: FLUXNET2015 CA-TP2 Ontario - Turkey Point 1989 Plantation White Pine, 2016a.

Arain, M. A.: FLUXNET2015 CA-TP1 Ontario - Turkey Point 2002 Plantation White Pine, 2016b.

Arain, M. A.: FLUXNET2015 CA-TP4 Ontario - Turkey Point 1939 Plantation White Pine, 2016c.

Ardö, J., El Tahir, B. A., and ElKhidir, H. A. M.: FLUXNET2015 SD-Dem Demokeya, 2016.

640   Arndt, S., Hinko-Najera, N., and Griebel, A.: FLUXNET2015 AU-Wom Wombat, 2016.

Aurela, M., Lohila, A., Tuovinen, J.-P., Hatakka, J., Rainne, J., Mäkelä, T., and Lauria, T.: FLUXNET2015 FI-Lom Lompolojankka, 2016a.

Aurela, M., Tuovinen, J.-P., Hatakka, J., Lohila, A., Mäkelä, T., Rainne, J., and Lauria, T.: FLUXNET2015 FI-Sod Sodankyla, 2016b.

Badgley, G., Field, C. B., and Berry, J. A.: Canopy Near-Infrared Reflectance and Terrestrial Photosynthesis, Science Advances, 3, 2017.

Baker, J. and Griffis, T.: AmeriFlux FLUXNET-1F US-Ro5 Rosemount I18_South, 2021.

645   Baker, J. and Griffis, T.: AmeriFlux FLUXNET-1F US-Ro4 Rosemount Prairie, 2022a.

Baker, J. and Griffis, T.: AmeriFlux FLUXNET-1F US-Ro6 Rosemount I18_North, 2022b.

Baker, J., Griffis, T., and Griffis, T.: AmeriFlux FLUXNET-1F US-Ro1 Rosemount- G21, 2022.

Baldocchi, D.: FLUXNET2015 US-Twt Twitchell Island, 2016.

Baldocchi, D. and Ma, S.: FLUXNET2015 US-Ton Tonzi Ranch, 2016.

650   Baldocchi, D. and Penuelas, J.: The Physics and Ecology of Mining Carbon Dioxide from the Atmosphere by Ecosystems, Global Change Biology, 25, 1191–1197, 2019.

Baldocchi, D., Ma, S., and Xu, L.: FLUXNET2015 US-Var Vaira Ranch- Ione, 2016.

Baldocchi, D. D.: How Eddy Covariance Flux Measurements Have Contributed to Our Understanding of *Global Change Biology*, Global Change Biology, 26, 242–260, 2019.

655   Bao, S., Wutzler, T., Koirala, S., Cuntz, M., Ibrom, A., Besnard, S., Walther, S., Šigut, L., Moreno, A., Weber, U., Wohlfahrt, G., Cleverly, J., Migliavacca, M., Woodgate, W., Merbold, L., Veenendaal, E., and Carvalhais, N.: Environment-Sensitivity Functions for Gross Primary Productivity in Light Use Efficiency Models, Agricultural and Forest Meteorology, 312, 108 708, 2022.

Belelli, L., Papale, D., and Valentini, R.: FLUXNET2015 RU-Ha1 Hakasia Steppe, 2016.

Berbigier, P. and Loustau, D.: FLUXNET2015 FR-LBr Le Bray, 2016.

660   Berg, A. and Sheffield, J.: Evapotranspiration Partitioning in CMIP5 Models: Uncertainties and Future Projections, Journal of Climate, 32, 2653–2671, 2019.

Beringer, J. and Hutley, L.: FLUXNET2015 AU-Fog Fogg Dam, 2016a.

Beringer, J. and Hutley, L.: FLUXNET2015 AU-DaP Daly River Savanna, 2016b.

Beringer, J. and Hutley, L.: FLUXNET2015 AU-Ade Adelaide River, 2016c.

665   Beringer, J. and Hutley, L.: FLUXNET2015 AU-RDF Red Dirt Melon Farm, Northern Territory, 2016d.

Beringer, J. and Hutley, L.: FLUXNET2015 AU-Dry Dry River, 2016e.

Beringer, J. and Hutley, P. L.: FLUXNET2015 AU-DaS Daly River Cleared, 2016f.

Beringer, J. and Walker, J.: FLUXNET2015 AU-Ync Jaxa, 2016.

Beringer, J., Cunningham, S., Baker, P., Cavagnaro, T., MacNally, R., Thompson, R., and McHugh, I.: FLUXNET2015 AU-Whr Whroo,
670   2016a.

Beringer, J., Hutley, L., McGuire, D., and U, P.: FLUXNET2015 AU-Wac Wallaby Creek, 2016b.

Bernhofer, C., Grünwald, T., Moderow, U., Hehn, M., Eichelmann, U., and Prasse, H.: FLUXNET2015 DE-Spw Spreewald, 2016.

Billesbach, D., Bradford, J., and Torn, M.: FLUXNET2015 US-AR2 ARM USDA UNL OSU Woodward Switchgrass 2, 2016a.

Billesbach, D., Bradford, J., and Torn, M.: FLUXNET2015 US-AR1 ARM USDA UNL OSU Woodward Switchgrass 1, 2016b.

675   Billesbach, D., Kueppers, L., Torn, M., and Biraud, S.: AmeriFlux FLUXNET-1F US-A32 ARM-SGP Medford Hay Pasture, 2022.

Biraud, S., Fischer, M., Chan, S., and Torn, M.: AmeriFlux FLUXNET-1F US-ARM ARM Southern Great Plains Site- Lamont, 2022.

Black, T.: AmeriFlux FLUXNET-1F CA-LP1 British Columbia - Mountain Pine Beetle-Attacked Lodgepole Pine Stand, 2021.

Black, T. A.: FLUXNET2015 CA-Obs Saskatchewan - Western Boreal, Mature Black Spruce, 2016a.

Black, T. A.: FLUXNET2015 CA-Oas Saskatchewan - Western Boreal, Mature Aspen, 2016b.

680   Blanken, P., Monson, R., Burns, S., Bowling, D., and Turnipseed, A.: AmeriFlux FLUXNET-1F US-NR1 Niwot Ridge Forest (LTER NWT1),
2022.

Bodesheim, P., Jung, M., Gans, F., Mahecha, M. D., and Reichstein, M.: Upscaled Diurnal Cycles of Land–Atmosphere Fluxes: A New
Global Half-Hourly Data Product, Earth System Science Data, 10, 1327–1365, 2018.

Bohrer, G.: AmeriFlux FLUXNET-1F US-ORv Olentangy River Wetland Research Park, 2021.

685   Bohrer, G.: AmeriFlux FLUXNET-1F US-UM3 Douglas Lake, 2022.

Bohrer, G. and Kerns, J.: AmeriFlux FLUXNET-1F US-OWC Old Woman Creek, 2022.

Boike, J., Westermann, S., Lüers, J., Langer, M., and Piel, K.: FLUXNET2015 SJ-Blv Bayelva, Spitsbergen, 2016.

Bonan, G. B., Lawrence, P. J., Oleson, K. W., Levis, S., Jung, M., Reichstein, M., Lawrence, D. M., and Swenson, S. C.: Improving Canopy
Processes in the Community Land Model Version 4 (CLM4) Using Global Flux Fields Empirically Inferred from FLUXNET Data, Journal
690   of Geophysical Research, 116, 2011.

Bowling, D.: FLUXNET2015 US-Cop Corral Pocket, 2016.

Brunsell, N.: AmeriFlux FLUXNET-1F US-KFS Kansas Field Station, 2022a.

Brunsell, N.: AmeriFlux FLUXNET-1F US-KLS Kansas Land Institute, 2022b.

Burton, C. A., Renzullo, L. J., Rifai, S. W., and Van Dijk, A. I. J. M.: Empirical Upscaling of OzFlux Eddy Covariance for High-Resolution
695   Monitoring of Terrestrial Carbon Uptake in Australia, 2023.

Byrne, B., Baker, D. F., Basu, S., Bertolacci, M., Bowman, K. W., Carroll, D., Chatterjee, A., Chevallier, F., Ciais, P., Cressie, N., Crisp,
D., Crowell, S., Deng, F., Deng, Z., Deutscher, N. M., Dubey, M. K., Feng, S., García, O. E., Griffith, D. W. T., Herkommer, B., Hu, L.,
Jacobson, A. R., Janardanan, R., Jeong, S., Johnson, M. S., Jones, D. B. A., Kivi, R., Liu, J., Liu, Z., Maksyutov, S., Miller, J. B., Miller,
S. M., Morino, I., Notholt, J., Oda, T., O'Dell, C. W., Oh, Y.-S., Ohyama, H., Patra, P. K., Peiro, H., Petri, C., Philip, S., Pollard, D. F.,
700   Poulter, B., Remaud, M., Schuh, A., Sha, M. K., Shiomi, K., Strong, K., Sweeney, C., Té, Y., Tian, H., Velazco, V. A., Vrekoussis, M.,
Warneke, T., Worden, J. R., Wunch, D., Yao, Y., Yun, J., Zammit-Mangion, A., and Zeng, N.: National CO_2 Budgets (2015–2020) Inferred
from Atmospheric CO_2 Observations in Support of the Global Stocktake, Earth System Science Data, 15, 963–1004, 2023.

Camps-Valls, G., Tuia, D., Zhu, X. X., and Reichstein, M.: Deep Learning for the Earth Sciences: A Comprehensive Approach to Remote Sensing, Climate Science, and Geosciences, Wiley, 1 edn., 2021.

705 Cescatti, A., Marcolla, B., Zorer, R., and Gianelle, D.: FLUXNET2015 IT-La2 Lavarone2, 2016.

Chamberlain, S., Oikawa, P., Sturtevant, C., Szutu, D., Verfaillie, J., and Baldocchi, D.: AmeriFlux FLUXNET-1F US-Tw3 Twitchell Alfalfa, 2022.

Chen, J.: FLUXNET2015 US-Wi5 Mixed Young Jack Pine (MYJP), 2016a.

Chen, J.: FLUXNET2015 US-Wi3 Mature Hardwood (MHW), 2016b.

710 Chen, J.: FLUXNET2015 US-Wi8 Young Hardwood Clearcut (YHW), 2016c.

Chen, J.: FLUXNET2015 US-Wi4 Mature Red Pine (MRP), 2016d.

Chen, J.: FLUXNET2015 US-Wi1 Intermediate Hardwood (IHW), 2016e.

Chen, J.: FLUXNET2015 US-Wi9 Young Jack Pine (YJP), 2016f.

Chen, J.: FLUXNET2015 US-Wi0 Young Red Pine (YRP), 2016g.

715 Chen, J.: FLUXNET2015 US-Wi6 Pine Barrens #1 (PB1), 2016h.

Chen, J.: FLUXNET2015 US-Wi7 Red Pine Clearcut (RPCC), 2016i.

Chen, J.: FLUXNET2015 US-Wi2 Intermediate Red Pine (IRP), 2016j.

Chen, J. and Chu, H.: FLUXNET2015 US-WPT Winous Point North Marsh, 2016a.

Chen, J. and Chu, H.: FLUXNET2015 US-CRT Curtice Walter-Berger Cropland, 2016b.

720 Chen, J., Chu, H., and Noormets, A.: FLUXNET2015 US-Oho Oak Openings, 2016.

Chen, S.: FLUXNET2015 CN-Du2 Duolun_grassland (D01), 2016k.

Chen, T. and Guestrin, C.: XGBoost, in: Proceedings of the 22nd ACM SIGKDD International Conference on Knowledge Discovery and Data Mining, ACM, 2016.

Christen, A. and Knox, S.: AmeriFlux FLUXNET-1F CA-DBB Delta Burns Bog, 2022.

725 Christensen, T.: FLUXNET2015 SJ-Adv Adventdalen, 2016.

Cleverly, J. and Eamus, D.: FLUXNET2015 AU-TTE Ti Tree East, 2016a.

Cleverly, J. and Eamus, D.: FLUXNET2015 AU-ASM Alice Springs, 2016b.

Coenders-Gerrits, A. M. J., van der Ent, R. J., Bogaard, T. A., Wang-Erlandsson, L., Hrachowitz, M., and Savenije, H. H. G.: Uncertainties in Transpiration Estimates, Nature, 506, E1–E2, 2014.

730 Dannenberg, M. P., Barnes, M. L., Smith, W. K., Johnston, M. R., Meerdink, S. K., Wang, X., Scott, R. L., and Biederman, J. A.: Upscaling Dryland Carbon and Water Fluxes with Artificial Neural Networks of Optical, Thermal, and Microwave Satellite Remote Sensing, Biogeosciences, 20, 383–404, 2023.

Desai, A.: FLUXNET2015 US-WCr Willow Creek, 2016a.

Desai, A.: FLUXNET2015 US-Syv Sylvania Wilderness Area, 2016b.

735 Desai, A.: FLUXNET2015 US-Los Lost Creek, 2016c.

Desai, A.: FLUXNET2015 US-PFa Park Falls/WLEF, 2016d.

Desai, A.: AmeriFlux FLUXNET-1F US-CS1 Central Sands Irrigated Agricultural Field, 2022a.

Desai, A.: AmeriFlux FLUXNET-1F US-CS4 Central Sands Irrigated Agricultural Field, 2022b.

Desai, A.: AmeriFlux FLUXNET-1F US-CS2 Tri County School Pine Forest, 2022c.

740 Desai, A.: AmeriFlux FLUXNET-1F US-CS3 Central Sands Irrigated Agricultural Field, 2022d.

Dolman, H., Hendriks, D., Parmentier, F.-J., Marchesini, L. B., Dean, J., and Van Huissteden, K.: FLUXNET2015 NL-Hor Horstermeer, 2016a.

Dolman, H., Van Der Molen, M., Parmentier, F.-J., Marchesini, L. B., Dean, J., Van Huissteden, K., and Maximov, T.: FLUXNET2015 RU-Cok Chokurdakh, 2016b.

745   Dong, G.: FLUXNET2015 CN-Cng Changling, 2016.

Drake, B. and Hinkle, R.: FLUXNET2015 US-KS1 Kennedy Space Center (Slash Pine), 2016a.

Drake, B. and Hinkle, R.: FLUXNET2015 US-KS2 Kennedy Space Center (Scrub Oak), 2016b.

Euskirchen, E.: AmeriFlux FLUXNET-1F US-BZo Bonanza Creek Old Thermokarst Bog, 2022a.

Euskirchen, E.: AmeriFlux FLUXNET-1F US-BZB Bonanza Creek Thermokarst Bog, 2022b.

750   Euskirchen, E.: AmeriFlux FLUXNET-1F US-BZF Bonanza Creek Rich Fen, 2022c.

Euskirchen, E.: AmeriFlux FLUXNET-1F US-BZS Bonanza Creek Black Spruce, 2022d.

Euskirchen, E., Shaver, G., and Bret-Harte, S.: AmeriFlux FLUXNET-1F US-ICs Imnavait Creek Watershed Wet Sedge Tundra, 2022a.

Euskirchen, E., Shaver, G., and Bret-Harte, S.: AmeriFlux FLUXNET-1F US-ICt Imnavait Creek Watershed Tussock Tundra, 2022b.

Ewers, B. and Pendall, E.: FLUXNET2015 US-Sta Saratoga, 2016.

755   Fares, S.: FLUXNET2015 US-Lin Lindcove Orange Orchard, 2016.

Flerchinger, G.: AmeriFlux FLUXNET-1F US-Rwf RCEW Upper Sheep Prescibed Fire, 2022a.

Flerchinger, G.: AmeriFlux FLUXNET-1F US-Rws Reynolds Creek Wyoming Big Sagebrush, 2022b.

Flerchinger, G.: AmeriFlux FLUXNET-1F US-Rms RCEW Mountain Big Sagebrush, 2022c.

Flerchinger, G. and Reba, M.: AmeriFlux FLUXNET-1F US-Rwe RCEW Reynolds Mountain East, 2022.

760   Forsythe, J., Kline, M., and O'Halloran, T.: AmeriFlux FLUXNET-1F US-HB1 North Inlet Crab Haul Creek, 2021.

Franssen, H. H., Stöckli, R., Lehner, I., Rotenberg, E., and Seneviratne, S.: Energy balance closure of eddy-covariance data: A multisite analysis for European FLUXNET stations, Agricultural and Forest Meteorology, 150, 1553–1567, https://doi.org/10.1016/j.agrformet.2010.08.005, 2010.

Fratini, G., McDermitt, D. K., and Papale, D.: Eddy-covariance flux errors due to biases in gas concentration measurements: origins, quan-
765   tification and correction, Biogeosciences, 11, 1037–1051, https://doi.org/10.5194/bg-11-1037-2014, 2014.

Friedl, M. and Sulla-Menashe, D.: MCD12C1 MODIS/Terra+Aqua Land Cover Type Yearly L3 Global 0.05Deg CMG V006, https://doi.org/https://doi.org/10.5067/MODIS/MCD12C1.006, 2015.

Fu, Z., Gerken, T., Bromley, G., Araújo, A., Bonal, D., Burban, B., Ficklin, D., Fuentes, J. D., Goulden, M., Hirano, T., Kosugi, Y., Liddell, M., Nicolini, G., Niu, S., Roupsard, O., Stefani, P., Mi, C., Tofte, Z., Xiao, J., Valentini, R., Wolf, S., and Stoy, P. C.: The Surface-
770   Atmosphere Exchange of Carbon Dioxide in Tropical Rainforests: Sensitivity to Environmental Drivers and Flux Measurement Methodology, Agricultural and Forest Meteorology, 263, 292–307, 2018.

Gao, B.-c.: NDWI—A Normalized Difference Water Index for Remote Sensing of Vegetation Liquid Water from Space, Remote Sensing of Environment, 58, 257–266, 1996.

Garcia, A., Di Bella, C., Houspanossian, J., Magliano, P., Jobbágy, E., Posse, G., Fernández, R., and Nosetto, M.: FLUXNET2015 AR-SLu
775   San Luis, 2016.

Gash, J. H. C.: An Analytical Model of Rainfall Interception by Forests, Quarterly Journal of the Royal Meteorological Society, 105, 43–55, 1979.

Goldstein, A.: FLUXNET2015 US-Blo Blodgett Forest, 2016.

Good, S. P., Noone, D., and Bowen, G.: Hydrologic Connectivity Constrains Partitioning of Global Terrestrial Water Fluxes, Science, 349, 175–177, 2015.

Goslee, S.: AmeriFlux FLUXNET-1F US-HWB USDA ARS Pasture Sytems and Watershed Management Research Unit- Hawbecker Site, 2022.

Gough, C., Bohrer, G., and Curtis, P.: FLUXNET2015 US-UMB Univ. Of Mich. Biological Station, 2016.

Gough, C., Bohrer, G., and Curtis, P.: AmeriFlux FLUXNET-1F US-UMd UMBS Disturbance, 2022.

Goulden, M.: FLUXNET2015 CA-NS2 UCI-1930 Burn Site, 2016a.

Goulden, M.: FLUXNET2015 CA-NS3 UCI-1964 Burn Site, 2016b.

Goulden, M.: FLUXNET2015 CA-NS4 UCI-1964 Burn Site Wet, 2016c.

Goulden, M.: FLUXNET2015 BR-Sa3 Santarem-Km83-Logged Forest, 2016d.

Goulden, M.: FLUXNET2015 CA-NS6 UCI-1989 Burn Site, 2016e.

Goulden, M.: FLUXNET2015 CA-NS7 UCI-1998 Burn Site, 2016f.

Goulden, M.: FLUXNET2015 CA-NS5 UCI-1981 Burn Site, 2016g.

Griffis, T. and Roman, T.: AmeriFlux FLUXNET-1F PE-QFR Quistococha Forest Reserve, 2021.

Gruening, C., Goded, I., Cescatti, A., Manca, G., and Seufert, G.: FLUXNET2015 IT-SRo San Rossore, 2016a.

Gruening, C., Goded, I., Cescatti, A., and Pokorska, O.: FLUXNET2015 IT-Isp Ispra ABC-IS, 2016b.

Hansen, B. U.: FLUXNET2015 GL-NuF Nuuk Fen, 2016.

Heinsch, F., Zhao, M., Running, S., Kimball, J., Nemani, R., Davis, K., Bolstad, P., Cook, B., Desai, A., Ricciuto, D., Law, B., Oechel, W., Kwon, H., Luo, H., Wofsy, S., Dunn, A., Munger, J., Baldocchi, D., Xu, L., Hollinger, D., Richardson, A., Stoy, P., Siqueira, M., Monson, R., Burns, S., and Flanagan, L.: Evaluation of Remote Sensing Based Terrestrial Productivity from MODIS Using Regional Tower Eddy Flux Network Observations, IEEE Transactions on Geoscience and Remote Sensing, 44, 1908–1925, 2006.

Hersbach, H., Bell, B., Berrisford, P., Hirahara, S., Horányi, A., Muñoz-Sabater, J., Nicolas, J., Peubey, C., Radu, R., Schepers, D., Simmons, A., Soci, C., Abdalla, S., Abellan, X., Balsamo, G., Bechtold, P., Biavati, G., Bidlot, J., Bonavita, M., Chiara, G., Dahlgren, P., Dee, D., Diamantakis, M., Dragani, R., Flemming, J., Forbes, R., Fuentes, M., Geer, A., Haimberger, L., Healy, S., Hogan, R. J., Hólm, E., Janisková, M., Keeley, S., Laloyaux, P., Lopez, P., Lupu, C., Radnoti, G., Rosnay, P., Rozum, I., Vamborg, F., Villaume, S., and Thépaut, J.: The ERA5 Global Reanalysis, Quarterly Journal of the Royal Meteorological Society, 146, 1999–2049, 2020.

Hinkle, R.: AmeriFlux FLUXNET-1F US-KS3 Kennedy Space Center (Salt Marsh), 2022.

Hollinger, D.: AmeriFlux FLUXNET-1F US-Ho2 Howland Forest (West Tower), 2022.

Huang, X., Xiao, J., Wang, X., and Ma, M.: Improving the Global MODIS GPP Model by Optimizing Parameters with FLUXNET Data, Agricultural and Forest Meteorology, 300, 108 314, 2021.

Huete, A., Didan, K., Miura, T., Rodriguez, E., Gao, X., and Ferreira, L.: Overview of the Radiometric and Biophysical Performance of the MODIS Vegetation Indices, Remote Sensing of Environment, 83, 195–213, 2002.

Huggins, D.: AmeriFlux FLUXNET-1F US-CF1 CAF-LTAR Cook East, 2021.

Huggins, D.: AmeriFlux FLUXNET-1F US-CF3 CAF-LTAR Boyd North, 2022a.

Huggins, D.: AmeriFlux FLUXNET-1F US-CF4 CAF-LTAR Boyd South, 2022b.

Huggins, D.: AmeriFlux FLUXNET-1F US-CF2 CAF-LTAR Cook West, 2022c.

Ichii, K., Ueyama, M., Kondo, M., Saigusa, N., Kim, J., Alberto, M. C., Ardö, J., Euskirchen, E. S., Kang, M., Hirano, T., Joiner, J., Kobayashi, H., Marchesini, L. B., Merbold, L., Miyata, A., Saitoh, T. M., Takagi, K., Varlagin, A., Bret-Harte, M. S., Kitamura, K.,

Kosugi, Y., Kotani, A., Kumar, K., Li, S., Machimura, T., Matsuura, Y., Mizoguchi, Y., Ohta, T., Mukherjee, S., Yanagi, Y., Yasuda, Y., Zhang, Y., and Zhao, F.: New Data-driven Estimation of Terrestrial CO_2 fluxes in Asia Using a Standardized Database of Eddy Covariance Measurements, Remote Sensing Data, and Support Vector Regression, Journal of Geophysical Research: Biogeosciences, 122, 767–795, 2017.

Joiner, J. and Yoshida, Y.: Satellite-Based Reflectances Capture Large Fraction of Variability in Global Gross Primary Production (GPP) at Weekly Time Scales, Agricultural and Forest Meteorology, 291, 108 092, 2020.

Jung, M., Reichstein, M., and Bondeau, A.: Towards Global Empirical Upscaling of FLUXNET Eddy Covariance Observations: Validation of a Model Tree Ensemble Approach Using a Biosphere Model, Biogeosciences, 6, 2001–2013, 2009.

Jung, M., Reichstein, M., Margolis, H. A., Cescatti, A., Richardson, A. D., Arain, M. A., Arneth, A., Bernhofer, C., Bonal, D., Chen, J., Gianelle, D., Gobron, N., Kiely, G., Kutsch, W., Lasslop, G., Law, B. E., Lindroth, A., Merbold, L., Montagnani, L., Moors, E. J., Papale, D., Sottocornola, M., Vaccari, F., and Williams, C.: Global Patterns of Land-Atmosphere Fluxes of Carbon Dioxide, Latent Heat, and Sensible Heat Derived from Eddy Covariance, Satellite, and Meteorological Observations, Journal of Geophysical Research, 116, 2011.

Jung, M., Reichstein, M., Schwalm, C. R., Huntingford, C., Sitch, S., Ahlström, A., Arneth, A., Camps-Valls, G., Ciais, P., Friedlingstein, P., Gans, F., Ichii, K., Jain, A. K., Kato, E., Papale, D., Poulter, B., Raduly, B., Rödenbeck, C., Tramontana, G., Viovy, N., Wang, Y.-P., Weber, U., Zaehle, S., and Zeng, N.: Compensatory Water Effects Link Yearly Global Land CO2 Sink Changes to Temperature, Nature, 541, 516–520, 2017.

Jung, M., Koirala, S., Weber, U., Ichii, K., Gans, F., Camps-Valls, G., Papale, D., Schwalm, C., Tramontana, G., and Reichstein, M.: The FLUXCOM Ensemble of Global Land-Atmosphere Energy Fluxes, Scientific Data, 6, 2019.

Jung, M., Schwalm, C., Migliavacca, M., Walther, S., Camps-Valls, G., Koirala, S., Anthoni, P., Besnard, S., Bodesheim, P., Carvalhais, N., Chevallier, F., Gans, F., Goll, D. S., Haverd, V., Köhler, P., Ichii, K., Jain, A. K., Liu, J., Lombardozzi, D., Nabel, J. E. M. S., Nelson, J. A., O'Sullivan, M., Pallandt, M., Papale, D., Peters, W., Pongratz, J., Rödenbeck, C., Sitch, S., Tramontana, G., Walker, A., Weber, U., and Reichstein, M.: Scaling Carbon Fluxes from Eddy Covariance Sites to Globe: Synthesis and Evaluation of the FLUXCOM Approach, Biogeosciences, 17, 1343–1365, 2020.

Jung, M., Nelson, J., Migliavacca, M., El-Madany, T., Papale, D., Reichstein, M., Walther, S., and Wutzler, T.: Technical note: Flagging inconsistencies in flux tower data, Biogeosciences, 21, 1827–1846, https://doi.org/10.5194/bg-21-1827-2024, 2024.

Klatt, J., Schmid, H. P., Mauder, M., and Steinbrecher, R.: FLUXNET2015 DE-SfN Schechenfilz Nord, 2016.

Knohl, A., Tiedemann, F., Kolle, O., Schulze, E.-D., Anthoni, P., Kutsch, W., Herbst, M., and Siebicke, L.: FLUXNET2015 DE-Lnf Leine-felde, 2016.

Knox, S.: AmeriFlux FLUXNET-1F CA-DB2 Delta Burns Bog 2, 2022.

Kobayashi, H. and Suzuki, R.: FLUXNET2015 US-Prr Poker Flat Research Range Black Spruce Forest, 2016.

Kosugi, Y. and Takanashi, S.: FLUXNET2015 MY-PSO Pasoh Forest Reserve (PSO), 2016.

Kotani, A.: FLUXNET2015 JP-SMF Seto Mixed Forest Site, 2016a.

Kotani, A.: FLUXNET2015 JP-MBF Moshiri Birch Forest Site, 2016b.

Kumar, J., Hoffman, F. M., Hargrove, W. W., and Collier, N.: Understanding the Representativeness of FLUXNET for Upscaling carbon Flux from Eddy Covariance Measurements, 2016.

Kurc, S.: AmeriFlux FLUXNET-1F US-SRC Santa Rita Creosote, 2022.

Kusak, K., Sanchez, C., Szutu, D., and Baldocchi, D.: AmeriFlux FLUXNET-1F US-Snf Sherman Barn, 2022.

Kutzbach, L.: AmeriFlux FLUXNET-1F AR-TF1 Rio Moat Bog, 2021.

855 Köhler, P., Frankenberg, C., Magney, T. S., Guanter, L., Joiner, J., and Landgraf, J.: Global Retrievals of Solar-Induced Chlorophyll Fluores-
        cence With TROPOMI: First Results and Intersensor Comparison to OCO-2, Geophysical Research Letters, 45, 2018.

Law, B.: FLUXNET2015 US-Me3 Metolius-second Young Aged Pine, 2016a.

Law, B.: FLUXNET2015 US-Me6 Metolius Young Pine Burn, 2016b.

Law, B.: FLUXNET2015 US-Me1 Metolius - Eyerly Burn, 2016c.

860 Law, B.: FLUXNET2015 US-Me5 Metolius-first Young Aged Pine, 2016d.

Law, B.: FLUXNET2015 US-Me4 Metolius-old Aged Ponderosa Pine, 2016e.

Law, B.: AmeriFlux FLUXNET-1F US-Me2 Metolius Mature Ponderosa Pine, 2022.

Leuning, R., van Gorsel, E., Massman, W. J., and Isaac, P. R.: Reflections on the surface energy imbalance problem, Agricultural and Forest
        Meteorology, 156, 65–74, https://doi.org/https://doi.org/10.1016/j.agrformet.2011.12.002, 2012.

865 Liddell, M. J.: FLUXNET2015 AU-Rob Robson Creek, Queensland, Australia, 2016.

Lindauer, M., Steinbrecher, R., Wolpert, B., Mauder, M., and Schmid, H. P.: FLUXNET2015 DE-Lkb Lackenberg, 2016.

Litvak, M.: AmeriFlux FLUXNET-1F US-Mpj Mountainair Pinyon-Juniper Woodland, 2021.

Litvak, M.: AmeriFlux FLUXNET-1F US-Wjs Willard Juniper Savannah, 2022.

Liu, H., Huang, M., and Chen, X.: AmeriFlux FLUXNET-1F US-Hn3 Hanford 100H Sagebrush, 2022.

870 Lohila, A., Aurela, M., Tuovinen, J.-P., Hatakka, J., and Laurila, T.: FLUXNET2015 FI-Jok Jokioinen, 2016.

Lund, M., Jackowicz-Korczyński, M., and Abermann, J.: FLUXNET2015 GL-ZaH Zackenberg Heath, 2016a.

Lund, M., Jackowicz-Korczyński, M., and Abermann, J.: FLUXNET2015 GL-ZaF Zackenberg Fen, 2016b.

Macfarlane, C., Lambert, P., Byrne, J., Johnstone, C., and Smart, N.: FLUXNET2015 AU-Gin Gingin, 2016.

Manca, G. and Goded, I.: FLUXNET2015 IT-PT1 Parco Ticino Forest, 2016.

875 Margolis, H. A.: FLUXNET2015 CA-Qfo Quebec - Eastern Boreal, Mature Black Spruce, 2016.

Martens, B., Miralles, D. G., Lievens, H., van der Schalie, R., de Jeu, R. A. M., Fernández-Prieto, D., Beck, H. E., Dorigo, W. A., and
        Verhoest, N. E. C.: GLEAM V3: Satellite-Based Land Evaporation and Root-Zone Soil Moisture, Geoscientific Model Development, 10,
        1903–1925, 2017.

Massman, B.: FLUXNET2015 US-GBT GLEES Brooklyn Tower, 2016.

880 Massman, B.: AmeriFlux FLUXNET-1F US-GLE GLEES, 2022.

Matamala, R.: FLUXNET2015 US-IB2 Fermi National Accelerator Laboratory- Batavia (Prairie Site), 2016.

Matteucci, G.: FLUXNET2015 IT-Col Collelongo, 2016.

Mauder, M., Foken, T., and Cuxart, J.: Surface-Energy-Balance Closure over Land: A Review, Boundary-Layer Meteorology, 177, 395–426,
        https://doi.org/10.1007/s10546-020-00529-6, 2020.

885 McCaughey, H.: FLUXNET2015 CA-Gro Ontario - Groundhog River, Boreal Mixedwood Forest, 2016.

McGloin, R., Šigut, L., Havránková, K., Dušek, J., Pavelka, M., and Sedlák, P.: Energy balance closure at a vari-
        ety of ecosystems in Central Europe with contrasting topographies, Agricultural and Forest Meteorology, 248, 418–431,
        https://doi.org/10.1016/j.agrformet.2017.10.003, 2018.

Merbold, L., Rebmann, C., and Corradi, C.: FLUXNET2015 RU-Che Cherski, 2016.

890 Meyer, W., Cale, P., Koerber, G., Ewenz, C., and Sun, Q.: FLUXNET2015 AU-Cpr Calperum, 2016.

Meyers, T.: FLUXNET2015 US-LWW Little Washita Watershed, 2016a.

Meyers, T.: FLUXNET2015 US-Goo Goodwin Creek, 2016b.

Miralles, D. G., Holmes, T. R. H., De Jeu, R. A. M., Gash, J. H., Meesters, A. G. C. A., and Dolman, A. J.: Global Land-Surface Evaporation Estimated from Satellite-Based Observations, Hydrology and Earth System Sciences, 15, 453–469, 2011.

895 Miralles, D. G., Jiménez, C., Jung, M., Michel, D., Ershadi, A., McCabe, M. F., Hirschi, M., Martens, B., Dolman, A. J., Fisher, J. B., Mu, Q., Seneviratne, S. I., Wood, E. F., and Fernández-Prieto, D.: The WACMOS-ET Project – Part 2: Evaluation of Global Terrestrial Evaporation Data Sets, Hydrology and Earth System Sciences, 20, 823–842, 2016.

Moncrieff, J., Malhi, Y., and Leuning, R.: The Propagation of Errors in Long-Term Measurements of Land-Atmosphere Fluxes of Carbon and Water, Global Change Biology, 2, 231–240, 1996.

900 Munassar, S., Rödenbeck, C., Koch, F.-T., Totsche, K. U., Gałkowski, M., Walther, S., and Gerbig, C.: Net Ecosystem Exchange (NEE) Estimates 2006–2019 over Europe from a Pre-Operational Ensemble-Inversion System, Atmospheric Chemistry and Physics, 22, 7875–7892, 2022.

Munger, J. W.: FLUXNET2015 US-Ha1 Harvard Forest EMS Tower (HFR1), 2016.

Musavi, T., Migliavacca, M., Reichstein, M., Kattge, J., Wirth, C., Black, T. A., Janssens, I., Knohl, A., Loustau, D., Roupsard, O., Varlagin,
905 A., Rambal, S., Cescatti, A., Gianelle, D., Kondo, H., Tamrakar, R., and Mahecha, M. D.: Stand Age and Species Richness Dampen Interannual Variation of Ecosystem-Level Photosynthetic Capacity, Nature Ecology & Evolution, 1, 2017.

Nash, J. and Sutcliffe, J.: River Flow Forecasting Through Conceptual Models Part I — A Discussion of Principles, Journal of Hydrology, 10, 282–290, 1970.

Nelson, J.: Jnelson18/TranspirationEstimationAlgorithm: Small Bug Fixes with Compatability, Zenodo, 2021.

910 Nelson, J. A., Carvalhais, N., Cuntz, M., Delpierre, N., Knauer, J., Ogée, J., Migliavacca, M., Reichstein, M., and Jung, M.: Coupling Water and Carbon Fluxes to Constrain Estimates of Transpiration: The TEA Algorithm, Journal of Geophysical Research: Biogeosciences, 123, 3617–3632, 2018.

Nelson, J. A., Pérez-Priego, O., Zhou, S., Poyatos, R., Zhang, Y., Blanken, P. D., Gimeno, T. E., Wohlfahrt, G., Desai, A. R., Gioli, B., Limousin, J., Bonal, D., Paul-Limoges, E., Scott, R. L., Varlagin, A., Fuchs, K., Montagnani, L., Wolf, S., Delpierre, N., Berveiller,
915 D., Gharun, M., Belelli Marchesini, L., Gianelle, D., Šigut, L., Mammarella, I., Siebicke, L., Andrew Black, T., Knohl, A., Hörtnagl, L., Magliulo, V., Besnard, S., Weber, U., Carvalhais, N., Migliavacca, M., Reichstein, M., and Jung, M.: Ecosystem Transpiration and Evaporation: Insights from Three Water Flux Partitioning Methods Across FLUXNET Sites, Global Change Biology, 26, 6916–6930, 2020.

Network), N.: AmeriFlux FLUXNET-1F US-xBR NEON Bartlett Experimental Forest (BART), 2022.

920 Nouvellon, Y.: FLUXNET2015 CG-Tch Tchizalamou, 2016.

Novick, K. and Phillips, R.: AmeriFlux FLUXNET-1F US-MMS Morgan Monroe State Forest, 2022.

Novick, K. A., Metzger, S., Anderegg, W. R. L., Barnes, M., Cala, D. S., Guan, K., Hemes, K. S., Hollinger, D. Y., Kumar, J., Litvak, M., Lombardozzi, D., Normile, C. P., Oikawa, P., Runkle, B. R. K., Torn, M., and Wiesner, S.: Informing Nature-based Climate Solutions for the United States with the Best-available Science, Global Change Biology, 28, 3778–3794, 2022.

925 Oikawa, P.: AmeriFlux FLUXNET-1F US-EDN Eden Landing Ecological Reserve, 2021.

Olesen, J.: FLUXNET2015 DK-Fou Foulum, 2016.

Ourcival, J.-M.: FLUXNET2015 FR-Pue Puechabon, 2016.

Papale, D. and Valentini, R.: A New Assessment of European Forests Carbon Exchanges by Eddy Fluxes and Artificial Neural Network Spatialization, Global Change Biology, 9, 525–535, 2003.

930 Papale, D., Reichstein, M., Aubinet, M., Canfora, E., Bernhofer, C., Kutsch, W., Longdoz, B., Rambal, S., Valentini, R., Vesala, T., and Yakir, D.: Towards a standardized processing of Net Ecosystem Exchange measured with eddy covariance technique: algorithms and uncertainty estimation, Biogeosciences, 3, 571–583, https://doi.org/10.5194/bg-3-571-2006, 2006.

Papale, D., Black, T. A., Carvalhais, N., Cescatti, A., Chen, J., Jung, M., Kiely, G., Lasslop, G., Mahecha, M. D., Margolis, H., Merbold, L., Montagnani, L., Moors, E., Olesen, J. E., Reichstein, M., Tramontana, G., Gorsel, E., Wohlfahrt, G., and Ráduly, B.: Effect of Spatial
935 Sampling from European Flux Towers for Estimating Carbon and Water Fluxes with Artificial Neural Networks, Journal of Geophysical Research: Biogeosciences, 120, 1941–1957, 2015.

Papale, D., Tirone, G., Valentini, R., Arriga, N., Belelli, L., Consalvo, C., Dore, S., Manca, G., Mazzenga, F., Sabbatini, S., and Stefani, P.: FLUXNET2015 IT-Ro2 Roccarespampani 2, 2016.

Pastorello, G., Trotta, C., Canfora, E., Chu, H., Christianson, D., Cheah, Y.-W., Poindexter, C., Chen, J., Elbashandy, A., Humphrey, M.,
940 Isaac, P., Polidori, D., Reichstein, M., Ribeca, A., van Ingen, C., Vuichard, N., Zhang, L., Amiro, B., Ammann, C., Arain, M. A., Ardö, J., Arkebauer, T., Arndt, S. K., Arriga, N., Aubinet, M., Aurela, M., Baldocchi, D., Barr, A., Beamesderfer, E., Marchesini, L. B., Bergeron, O., Beringer, J., Bernhofer, C., Berveiller, D., Billesbach, D., Black, T. A., Blanken, P. D., Bohrer, G., Boike, J., Bolstad, P. V., Bonal, D., Bonnefond, J.-M., Bowling, D. R., Bracho, R., Brodeur, J., Brümmer, C., Buchmann, N., Burban, B., Burns, S. P., Buysse, P., Cale, P., Cavagna, M., Cellier, P., Chen, S., Chini, I., Christensen, T. R., Cleverly, J., Collalti, A., Consalvo, C., Cook, B. D., Cook, D., Coursolle, C.,
945 Cremonese, E., Curtis, P. S., D'Andrea, E., da Rocha, H., Dai, X., Davis, K. J., Cinti, B. D., Grandcourt, A. d., Ligne, A. D., De Oliveira, R. C., Delpierre, N., Desai, A. R., Di Bella, C. M., Tommasi, P. d., Dolman, H., Domingo, F., Dong, G., Dore, S., Duce, P., Dufrêne, E., Dunn, A., Dušek, J., Eamus, D., Eichelmann, U., ElKhidir, H. A. M., Eugster, W., Ewenz, C. M., Ewers, B., Famulari, D., Fares, S., Feigenwinter, I., Feitz, A., Fensholt, R., Filippa, G., Fischer, M., Frank, J., Galvagno, M., Gharun, M., Gianelle, D., Gielen, B., Gioli, B., Gitelson, A., Goded, I., Goeckede, M., Goldstein, A. H., Gough, C. M., Goulden, M. L., Graf, A., Griebel, A., Gruening, C., Grünwald,
950 T., Hammerle, A., Han, S., Han, X., Hansen, B. U., Hanson, C., Hatakka, J., He, Y., Hehn, M., Heinesch, B., Hinko-Najera, N., Hörtnagl, L., Hutley, L., Ibrom, A., Ikawa, H., Jackowicz-Korczynski, M., Janouš, D., Jans, W., Jassal, R., Jiang, S., Kato, T., Khomik, M., Klatt, J., Knohl, A., Knox, S., Kobayashi, H., Koerber, G., Kolle, O., Kosugi, Y., Kotani, A., Kowalski, A., Kruijt, B., Kurbatova, J., Kutsch, W. L., Kwon, H., Launiainen, S., Laurila, T., Law, B., Leuning, R., Li, Y., Liddell, M., Limousin, J.-M., Lion, M., Liska, A. J., Lohila, A., López-Ballesteros, A., López-Blanco, E., Loubet, B., Loustau, D., Lucas-Moffat, A., Lüers, J., Ma, S., Macfarlane, C., Magliulo, V.,
955 Maier, R., Mammarella, I., Manca, G., Marcolla, B., Margolis, H. A., Marras, S., Massman, W., Mastepanov, M., Matamala, R., Matthes, J. H., Mazzenga, F., McCaughey, H., McHugh, I., McMillan, A. M. S., Merbold, L., Meyer, W., Meyers, T., Miller, S. D., Minerbi, S., Moderow, U., Monson, R. K., Montagnani, L., Moore, C. E., Moors, E., Moreaux, V., Moureaux, C., Munger, J. W., Nakai, T., Neirynck, J., Nesic, Z., Nicolini, G., Noormets, A., Northwood, M., Nosetto, M., Nouvellon, Y., Novick, K., Oechel, W., Olesen, J. E., Ourcival, J.-M., Papuga, S. A., Parmentier, F.-J., Paul-Limoges, E., Pavelka, M., Peichl, M., Pendall, E., Phillips, R. P., Pilegaard, K., Pirk, N., Posse, G.,
960 Powell, T., Prasse, H., Prober, S. M., Rambal, S., Rannik, U., Raz-Yaseef, N., Rebmann, C., Reed, D., Dios, V. R. d., Restrepo-Coupe, N., Reverter, B. R., Roland, M., Sabbatini, S., Sachs, T., Saleska, S. R., Sánchez-Cañete, E. P., Sanchez-Mejia, Z. M., Schmid, H. P., Schmidt, M., Schneider, K., Schrader, F., Schroder, I., Scott, R. L., Sedlák, P., Serrano-Ortíz, P., Shao, C., Shi, P., Shironya, I., Siebicke, L., Šigut, L., Silberstein, R., Sirca, C., Spano, D., Steinbrecher, R., Stevens, R. M., Sturtevant, C., Suyker, A., Tagesson, T., Takanashi, S., Tang, Y., Tapper, N., Thom, J., Tomassucci, M., Tuovinen, J.-P., Urbanski, S., Valentini, R., van der Molen, M., van Gorsel, E., van Huissteden,
965 K., Varlagin, A., Verfaillie, J., Vesala, T., Vincke, C., Vitale, D., Vygodskaya, N., Walker, J. P., Walter-Shea, E., Wang, H., Weber, R., Westermann, S., Wille, C., Wofsy, S., Wohlfahrt, G., Wolf, S., Woodgate, W., Li, Y., Zampedri, R., Zhang, J., Zhou, G., Zona, D., Agarwal,

D., Biraud, S., Torn, M., and Papale, D.: The FLUXNET2015 Dataset and the ONEFlux Processing Pipeline for Eddy Covariance Data, Scientific Data, 7, 225, 2020.

Pendall, E. and Griebel, A.: FLUXNET2015 AU-Cum Cumberland Plains, 2016.

970   Pilegaard, K. and Ibrom, A.: FLUXNET2015 DK-Eng Enghave, 2016.

Posse, G., Lewczuk, N., Richter, K., and Cristiano, P.: FLUXNET2015 AR-Vir Virasoro, 2016.

Poveda, F. D., Ballesteros, A. L., Cañete, E. P. S., Ortiz, P. S., Jiménez, M. R. M., Priego, O. P., and Kowalski, A. S.: FLUXNET2015 ES-Amo Amoladeras, 2016.

Priestley, C. H. B. and Taylor, R. J.: On the Assessment of Surface Heat Flux and Evaporation Using Large-Scale Parameters, Monthly
975   Weather Review, 100, 81–92, 1972.

Randerson, J., Van der werf, G., Giglio, L., Collatz, G., and Kasibhatla, P.: Global Fire Emissions Database, Version 4.1 (GFEDv4), 2017.

Rannik, U., Peltola, O., and Mammarella, I.: Random uncertainties of flux measurements by the eddy covariance technique, Atmospheric Measurement Techniques, 9, 5163–5181, https://doi.org/10.5194/amt-9-5163-2016, 2016.

Reichstein, M., Falge, E., Baldocchi, D., Papale, D., Aubinet, M., Berbigier, P., Bernhofer, C., Buchmann, N., Gilmanov, T., Granier, A.,
980   Grunwald, T., Havrankova, K., Ilvesniemi, H., Janous, D., Knohl, A., Laurila, T., Lohila, A., Loustau, D., Matteucci, G., Meyers, T., Miglietta, F., Ourcival, J.-M., Pumpanen, J., Rambal, S., Rotenberg, E., Sanz, M., Tenhunen, J., Seufert, G., Vaccari, F., Vesala, T., Yakir, D., and Valentini, R.: On the Separation of Net Ecosystem Exchange into Assimilation and Ecosystem Respiration: Review and Improved Algorithm, Global Change Biology, 11, 1424–1439, 2005.

Reichstein, M., Camps-Valls, G., Stevens, B., Jung, M., Denzler, J., Carvalhais, N., and Prabhat: Deep Learning and Process Understanding
985   for Data-Driven Earth System Science, Nature, 566, 195–204, 2019.

Reverter, B. R., Perez-Cañete, E. S., and Kowalski, A. S.: FLUXNET2015 ES-Ln2 Lanjaron-Salvage Logging, 2016a.

Reverter, B. R., Perez-Cañete, E. S., and Kowalski, A. S.: FLUXNET2015 ES-LgS Laguna Seca, 2016b.

Rey-Sanchez, C., Wang, C., Szutu, D., Hemes, K., Verfaillie, J., and Baldocchi, D.: AmeriFlux FLUXNET-1F US-Bi2 Bouldin Island Corn, 2022a.

990   Rey-Sanchez, C., Wang, C., Szutu, D., Shortt, R., Chamberlain, S., Verfaillie, J., and Baldocchi, D.: AmeriFlux FLUXNET-1F US-Bi1 Bouldin Island Alfalfa, 2022b.

RI, I.: Ecosystem Final Quality (L2) Product in ETC-Archive Format - Release 2021-1, 2021.

RI, I.: Ecosystem Final Quality (L2) Product in ETC-Archive Format - Release 2022-1, 2022.

Roedenbeck, C. and Heimann, M.: Jena CarboScope: Atmospheric CO2 Inversion, 2022.

995   Rödenbeck, C., Zaehle, S., Keeling, R., and Heimann, M.: How Does the Terrestrial Carbon Exchange Respond to Inter-Annual Climatic Variations? A Quantification Based on Atmospheric CO<sub>2</sub> Data, Biogeosciences, 15, 2481–2498, 2018.

Sabbatini, S., Arriga, N., Gioli, B., and Papale, D.: FLUXNET2015 IT-CA2 Castel d'Asso2, 2016a.

Sabbatini, S., Arriga, N., Matteucci, G., and Papale, D.: FLUXNET2015 IT-CA3 Castel d'Asso 3, 2016b.

1000   Sabbatini, S., Arriga, N., and Papale, D.: FLUXNET2015 IT-CA1 Castel d'Asso1, 2016c.

Sachs, T., Wille, C., Larmanou, E., and Franz, D.: FLUXNET2015 DE-Zrk Zarnekow, 2016.

Saleska, S.: FLUXNET2015 BR-Sa1 Santarem-Km67-Primary Forest, 2016.

Sanchez, C. R., Sturtevant, C., Szutu, D., Baldocchi, D., Eichelmann, E., and Knox, S.: FLUXNET2015 US-Tw4 Twitchell East End Wetland, 2016.

1005   Schaaf, C. and Wang, Z.: MCD43A2 MODIS/Terra+Aqua BRDF/Albedo Quality Daily L3 Global - 500m V006, 2015a.

Schaaf, C. and Wang, Z.: MCD43A4 MODIS/Terra+Aqua BRDF/Albedo Nadir BRDF Adjusted Ref Daily L3 Global - 500m V006, 2015b.

Schlesinger, W. H. and Jasechko, S.: Transpiration in the Global Water Cycle, Agricultural and Forest Meteorology, 189-190, 115–117, 2014.

Schneider, K. and Schmidt, M.: FLUXNET2015 DE-Seh Selhausen, 2016.

Schneider, U., Hänsel, S., Finger, P., Rustemeier, E., and Ziese, M.: GPCC Full Data Monthly Version 2022 at 0.25°: Monthly Land-Surface
1010   Precipitation from Rain-Gauges Built on GTS-based and Historic Data, 2022.

Schroder, I., Zegelin, S., Palu, T., and Feitz, A.: FLUXNET2015 AU-Emr Emerald, 2016.

Scott, R.: FLUXNET2015 US-SRG Santa Rita Grassland, 2016a.

Scott, R.: FLUXNET2015 US-SRM Santa Rita Mesquite, 2016b.

Scott, R.: FLUXNET2015 US-Wkg Walnut Gulch Kendall Grasslands, 2016c.

1015   Scott, R.: FLUXNET2015 US-Whs Walnut Gulch Lucky Hills Shrub, 2016d.

Shao, C.: FLUXNET2015 CN-Sw2 Siziwang Grazed (SZWG), 2016a.

Shao, C.: FLUXNET2015 CN-Du3 Duolun Degraded Meadow, 2016b.

Shi, P., Zhang, X., and He, Y.: FLUXNET2015 CN-Dan Dangxiong, 2016.

Shortt, R., Hemes, K., Szutu, D., Verfaillie, J., and Baldocchi, D.: AmeriFlux FLUXNET-1F US-Sne Sherman Island Restored Wetland,
1020   2022.

Sigut, L., Havrankova, K., Jocher, G., Pavelka, M., and Janouš, D.: FLUXNET2015 CZ-BK2 Bily Kriz Grassland, 2016.

Silveira, M.: AmeriFlux FLUXNET-1F US-ONA Florida Pine Flatwoods, 2021.

Soloway, A. D., Amiro, B. D., Dunn, A. L., and Wofsy, S. C.: Carbon neutral or a sink? Uncertainty caused by gap-filling
      long-term flux measurements for an old-growth boreal black spruce forest, Agricultural and Forest Meteorology, 233, 110–121,
1025   https://doi.org/10.1016/j.agrformet.2016.11.005, 2017.

Spano, D., Duce, P., Marras, S., Sirca, C., Arca, A., Zara, P., and Ventura, A.: FLUXNET2015 IT-Noe Arca Di Noe - Le Prigionette, 2016.

Staebler, R.: AmeriFlux FLUXNET-1F CA-Cbo Ontario - Mixed Deciduous, Borden Forest Site, 2022.

Stoy, P. C., Mauder, M., Foken, T., Marcolla, B., Boegh, E., Ibrom, A., Arain, M. A., Arneth, A., Aurela, M., Bernhofer, C., Cescatti, A.,
      Dellwik, E., Duce, P., Gianelle, D., van Gorsel, E., Kiely, G., Knohl, A., Margolis, H., McCaughey, H., Merbold, L., Montagnani, L.,
1030   Papale, D., Reichstein, M., Saunders, M., Serrano-Ortiz, P., Sottocornola, M., Spano, D., Vaccari, F., and Varlagin, A.: A data-driven
      analysis of energy balance closure across FLUXNET research sites: The role of landscape scale heterogeneity, Agricultural and Forest
      Meteorology, 171-172, 137–152, https://doi.org/10.1016/j.agrformet.2012.11.004, 2013.

Sturtevant, C., Szutu, D., Baldocchi, D., Matthes, J. H., Oikawa, P., and Chamberlain, S. D.: FLUXNET2015 US-Myb Mayberry Wetland,
      2016.

1035   Sturtevant, C., Verfaillie, J., and Baldocchi, D.: AmeriFlux FLUXNET-1F US-Tw2 Twitchell Corn, 2022.

Suyker, A.: FLUXNET2015 US-Ne3 Mead - Rainfed Maize-Soybean Rotation Site, 2016a.

Suyker, A.: FLUXNET2015 US-Ne2 Mead - Irrigated Maize-Soybean Rotation Site, 2016b.

Suyker, A.: AmeriFlux FLUXNET-1F US-Ne1 Mead - Irrigated Continuous Maize Site, 2022.

Tagesson, T., Ardö, J., and Fensholt, R.: FLUXNET2015 SN-Dhr Dahra, 2016.

1040   Tang, Y., Kato, T., and Du, M.: FLUXNET2015 CN-HaM Haibei Alpine Tibet Site, 2016.

Team, D. . and Centre, I. E. T.: Drought-2018 Ecosystem Eddy Covariance Flux Product for 52 Stations in FLUXNET-Archive Format, 2020.

Team, W. W. . and Centre, I. E. T.: Warm Winter 2020 Ecosystem Eddy Covariance Flux Product for 73 Stations in FLUXNET-Archive Format—Release 2022-1, 2022.

Torn, M.: FLUXNET2015 US-ARc ARM Southern Great Plains Control Site- Lamont, 2016a.

1045 Torn, M.: FLUXNET2015 US-ARb ARM Southern Great Plains Burn Site- Lamont, 2016b.

Torn, M. and Dengel, S.: AmeriFlux FLUXNET-1F US-NGB NGEE Arctic Barrow, 2021.

Tramontana, G., Jung, M., Schwalm, C. R., Ichii, K., Camps-Valls, G., Ráduly, B., Reichstein, M., Arain, M. A., Cescatti, A., Kiely, G., Merbold, L., Serrano-Ortiz, P., Sickert, S., Wolf, S., and Papale, D.: Predicting Carbon Dioxide and Energy Fluxes Across Global FLUXNET Sites with regression Algorithms, Biogeosciences, 13, 4291–4313, 2016.

1050 Turner, D. P., Ritts, W. D., Cohen, W. B., Gower, S. T., Running, S. W., Zhao, M., Costa, M. H., Kirschbaum, A. A., Ham, J. M., Saleska, S. R., and Ahl, D. E.: Evaluation of MODIS NPP and GPP Products Across Multiple Biomes, Remote Sensing of Environment, 102, 282–292, 2006.

Ukkola, A. M., Abramowitz, G., and De Kauwe, M. G.: A Flux Tower Dataset Tailored for Land Model Evaluation, Earth System Science Data, 14, 449–461, 2022.

1055 Upton, S., Reichstein, M., Gans, F., Peters, W., Kraft, B., and Bastos, A.: Constraining Biospheric Carbon Dioxide Fluxes by Combined Top-down and Bottom-up Approaches, 2023.

Valach, A., Shortt, R., Szutu, D., Eichelmann, E., Knox, S., Hemes, K., Verfaillie, J., and Baldocchi, D.: AmeriFlux FLUXNET-1F US-Tw1 Twitchell Wetland West Pond, 2021.

Valach, A., Kasak, K., Szutu, D., Verfaillie, J., and Baldocchi, D.: AmeriFlux FLUXNET-1F US-Tw5 East Pond Wetland, 2022.

1060 Valentini, R., Dore, S., Mazzenga, F., Sabbatini, S., Stefani, P., Tirone, G., and Papale, D.: FLUXNET2015 IT-Cpz Castelporziano, 2016a.

Valentini, R., Nicolini, G., Stefani, P., De Grandcourt, A., and Stivanello, S.: FLUXNET2015 GH-Ank Ankasa, 2016b.

Valentini, R., Tirone, G., Vitale, D., Papale, D., Arriga, N., Belelli, L., Dore, S., Manca, G., Mazzenga, F., Pegoraro, E., Sabbatini, S., and Stefani, P.: FLUXNET2015 IT-Ro1 Roccarespampani 1, 2016c.

Vekuri, H., Tuovinen, J.-P., Kulmala, L., Papale, D., Kolari, P., Aurela, M., Laurila, T., Liski, J., and Lohila, A.: A widely-used eddy covari-
1065 ance gap-filling method creates systematic bias in carbon balance estimates, Scientific Reports, 13, https://doi.org/10.1038/s41598-023-28827-2, 2023.

Virkkala, A., Aalto, J., Rogers, B. M., Tagesson, T., Treat, C. C., Natali, S. M., Watts, J. D., Potter, S., Lehtonen, A., Mauritz, M., Schuur, E. A. G., Kochendorfer, J., Zona, D., Oechel, W., Kobayashi, H., Humphreys, E., Goeckede, M., Iwata, H., Lafleur, P. M., Euskirchen, E. S., Bokhorst, S., Marushchak, M., Martikainen, P. J., Elberling, B., Voigt, C., Biasi, C., Sonnentag, O., Parmentier, F. W., Ueyama,
1070 M., Celis, G., St.Louis, V. L., Emmerton, C. A., Peichl, M., Chi, J., Järveoja, J., Nilsson, M. B., Oberbauer, S. F., Torn, M. S., Park, S., Dolman, H., Mammarella, I., Chae, N., Poyatos, R., López-Blanco, E., Christensen, T. R., Kwon, M. J., Sachs, T., Holl, D., and Luoto, M.: Statistical Upscaling of Ecosystem CO$_2$ fluxes Across the Terrestrial Tundra and Boreal Domain: Regional Patterns and Uncertainties, Global Change Biology, 27, 4040–4059, 2021.

Vitale, D., Fratini, G., Bilancia, M., Nicolini, G., Sabbatini, S., and Papale, D.: A robust data cleaning procedure for eddy covariance flux
1075 measurements, Biogeosciences, 17, 1367–1391, https://doi.org/10.5194/bg-17-1367-2020, 2020.

Vivoni, E. and Perez-Ruiz, E.: AmeriFlux FLUXNET-1F US-Jo2 Jornada Experimental Range Mixed Shrubland, 2022.

Vourlitis, G., Dalmagro, H., De S. Nogueira, J., Johnson, M., and Arruda, P.: AmeriFlux FLUXNET-1F BR-Npw Northern Pantanal Wetland, 2022.

Wagner-Riddle, C.: AmeriFlux FLUXNET-1F CA-ER1 Elora Research Station, 2021.

1080 Walther, S.: README FluxnetEO V2, 2023.

Walther and Besnard, Nelson, J. A., El-Many, T. S., Migliavacca, M., Weber, U., Carvalhais, N., Ermida, S. L., Brümmer, C., Schrader, F., Prokushkin, A. S., Panov, A. V., and Jung, M.: Technical Note: A View from Space on Global Flux Towers by MODIS and Landsat: The FluxnetEO Data Set, Biogeosciences, 19, 2805–2840, 2022.

Wan, Z., Hook, S., and Hulley, G.: MOD11C1 MODIS/Terra Land Surface Temperature/Emissivity Daily L3 Global 0.05Deg CMG V006, 1085 2015.

Wang, H. and Fu, X.: FLUXNET2015 CN-Qia Qianyanzhou, 2016.

Wei, Z., Yoshimura, K., Wang, L., Miralles, D. G., Jasechko, S., and Lee, X.: Revisiting the Contribution of Transpiration to Global Terrestrial Evapotranspiration, Geophysical Research Letters, 44, 2792–2801, 2017.

Wohlfahrt, G., Hammerle, A., and Hörtnagl, L.: FLUXNET2015 AT-Neu Neustift, 2016.

1090 Wolf, S., Eugster, W., and Buchmann, N.: FLUXNET2015 PA-SPs Sardinilla-Pasture, 2016a.

Wolf, S., Eugster, W., and Buchmann, N.: FLUXNET2015 PA-SPn Sardinilla Plantation, 2016b.

Wood, J. and Gu, L.: AmeriFlux FLUXNET-1F US-MOz Missouri Ozark Site, 2022.

Woodgate, W., Van Gorsel, E., and Leuning, R.: FLUXNET2015 AU-Tum Tumbarumba, 2016.

Xiao, J., Zhuang, Q., Baldocchi, D. D., Law, B. E., Richardson, A. D., Chen, J., Oren, R., Starr, G., Noormets, A., Ma, S., Verma, S. B., 1095 Wharton, S., Wofsy, S. C., Bolstad, P. V., Burns, S. P., Cook, D. R., Curtis, P. S., Drake, B. G., Falk, M., Fischer, M. L., Foster, D. R., Gu, L., Hadley, J. L., Hollinger, D. Y., Katul, G. G., Litvak, M., Martin, T. A., Matamala, R., McNulty, S., Meyers, T. P., Monson, R. K., Munger, J. W., Oechel, W. C., Paw U, K. T., Schmid, H. P., Scott, R. L., Sun, G., Suyker, A. E., and Torn, M. S.: Estimation of Net Ecosystem Carbon Exchange for the Conterminous United States by Combining MODIS and AmeriFlux Data, Agricultural and Forest Meteorology, 148, 1827–1847, 2008.

1100 Yao, Y., Li, Z., Wang, T., Chen, A., Wang, X., Du, M., Jia, G., Li, Y., Li, H., Luo, W., Ma, Y., Tang, Y., Wang, H., Wu, Z., Yan, J., Zhang, X., Zhang, Y., Zhang, Y., Zhou, G., and Piao, S.: A New Estimation of China's Net Ecosystem Productivity Based on Eddy Covariance Measurements and a Model Tree Ensemble Approach, Agricultural and Forest Meteorology, 253-254, 84–93, 2018.

Yepez, E. and Garatuza, J.: AmeriFlux FLUXNET-1F MX-Tes Tesopaco, Secondary Tropical Dry Forest, 2021.

Zhang, J. and Han, S.: FLUXNET2015 CN-Cha Changbaishan, 2016.

1105 Zhang, W., Jung, M., Migliavacca, M., Poyatos, R., Miralles, D. G., El-Many, T. S., Galvagno, M., Carrara, A., Arriga, N., Ibrom, A., Mammarella, I., Papale, D., Cleverly, J. R., Liddell, M., Wohlfahrt, G., Markwitz, C., Mauder, M., Paul-Limoges, E., Schmidt, M., Wolf, S., Brümmer, C., Arain, M. A., Fares, S., Kato, T., Ardö, J., Oechel, W., Hanson, C., Korkiakoski, M., Biraud, S., Steinbrecher, R., Billesbach, D., Montagnani, L., Woodgate, W., Shao, C., Carvalhais, N., Reichstein, M., and Nelson, J. A.: The effect of relative humidity on eddy covariance latent heat flux measurements and its implication for partitioning into transpiration and evaporation, Agricultural and 1110 Forest Meteorology, 330, https://doi.org/https://doi.org/10.1016/j.agrformet.2022.109305, 2023.

Zhang, Y., Xiao, X., Zhang, Y., Wolf, S., Zhou, S., Joiner, J., Guanter, L., Verma, M., Sun, Y., Yang, X., Paul-Limoges, E., Gough, C. M., Wohlfahrt, G., Gioli, B., van der Tol, C., Yann, N., Lund, M., and de Grandcourt, A.: On the Relationship Between Sub-Daily Instantaneous and Daily Total Gross Primary Production: Implications for Interpreting Satellite-Based SIF Retrievals, Remote Sensing of Environment, 205, 276–289, 2018.

1115 Zhao, M. and Running, S. W.: Drought-Induced Reduction in Global Terrestrial Net Primary Production from 2000 Through 2009, Science, 329, 940–943, 2010.

Zhou, G. and Yan, J.: FLUXNET2015 CN-Din Dinghushan, 2016.

Zhu, S., Quaife, T., and Hill, T.: Uniform upscaling techniques for eddy covariance FLUXes (UFLUX), International Journal of Remote Sensing, 45, 1450–1476, https://doi.org/10.1080/01431161.2024.2312266, 2024.

1120   Zona, D. and Oechel, W.: FLUXNET2015 US-Atq Atqasuk, 2016a.

Zona, D. and Oechel, W.: FLUXNET2015 US-Ivo Ivotuk, 2016b.

Zscheischler, J., Mahecha, M. D., Avitabile, V., Calle, L., Carvalhais, N., Ciais, P., Gans, F., Gruber, N., Hartmann, J., Herold, M., Ichii, K., Jung, M., Landschützer, P., Laruelle, G. G., Lauerwald, R., Papale, D., Peylin, P., Poulter, B., Ray, D., Regnier, P., Rödenbeck, C., Roman-Cuesta, R. M., Schwalm, C., Tramontana, G., Tyukavina, A., Valentini, R., van der Werf, G., West, T. O., Wolf, J. E., and Reichstein, M.:

1125   Reviews and Syntheses: An Empirical Spatiotemporal Description of the Global Surface–Atmosphere Carbon Fluxes: Opportunities and Data Limitations, Biogeosciences, 14, 3685–3703, 2017.